The role of aerodynamic resistance in thermal remote sensing-based evapotranspiration models

Ivonne Trebs [a,*], Kaniska Mallick [a,*], Nishan Bhattarai [b], Mauro Sulis [a], Jamie Cleverly [c,d], William Woodgate [e,f], Richard Silberstein [g,i], Nina Hinko-Najera [h], Jason Beringer [i], Wayne S. Meyer [j], Zhongbo Su [k], Gilles Boulet [l]

[a] Department of Environmental Research and Innovation, Luxembourg Institute of Science and Technology, Belvaux, Luxembourg
[b] School for Environment and Sustainability (SEAS), University of Michigan, Ann Arbor, USA
[c] School of Life Sciences, University of Technology Sydney, Broadway, NSW, Australia
[d] Terrestrial Ecosystem Research Network (TERN), College of Science and Engineering, James Cook University, Cairns, Qld, Australia
[e] CSIRO Land & Water, Canberra, ACT, Australia
[f] School of Earth and Environmental Science, University of Queensland, St Lucia, Australia
[g] Centre for Ecosystem Management, Edith Cowan University, Joondalup, WA, Australia
[h] School of Ecosystem and Forest Sciences, The University of Melbourne, Creswick, Australia
[i] School of Agriculture and Environment, University of Western Australia, Crawley, WA, Australia
[j] School of Biological Sciences, University of Adelaide, Adelaide, Australia
[k] University of Twente, Faculty of Geo-Information Science and Earth Observation (ITC), Enschede, the Netherlands
[l] CESBIO, Université de Toulouse, CNRS, CNES, UPS, IRD, INRAE, Toulouse, France

ARTICLE INFO

ABSTRACT

Aerodynamic resistance (hereafter r_a) is a preeminent variable in evapotranspiration (ET) modelling. The accurate quantification of r_a plays a pivotal role in determining the performance and consistency of thermal remote sensing-based surface energy balance (SEB) models for estimating ET at local to regional scales. Atmospheric stability links r_a with land surface temperature (LST) and the representation of their interactions in the SEB models determines the accuracy of ET estimates.

The present study investigates the influence of r_a and its relation to LST uncertainties on the performance of three structurally different SEB models. It used data from nine Australian OzFlux eddy covariance sites of contrasting aridity in conjunction with MODIS Terra and Aqua LST and leaf area index (LAI) products. Simulations of the sensible heat flux (H) and the latent heat flux (LE, the energy equivalent of ET in W/m^2) from the SPARSE (Soil Plant Atmosphere and Remote Sensing Evapotranspiration), SEBS (Surface Energy Balance System) and STIC (Surface Temperature Initiated Closure) models forced with MODIS LST, LAI, and in-situ meteorological datasets were evaluated against flux observations in water-limited (arid and semi-arid) and energy-limited (mesic) ecosystems from 2011 to 2019.

Our results revealed an overestimation tendency of instantaneous LE by all three models in the water-limited shrubland, woodland and grassland ecosystems by up to 50% on average, which was caused by an underestimation of H. Overestimation of LE was associated with discrepancies in r_a retrievals under conditions of high atmospheric instability, during which uncertainties in LST (expressed as the difference between MODIS LST and in-situ LST) apparently played a minor role. On the other hand, a positive difference in LST coincided with low r_a (high wind speeds) and caused a slight underestimation of LE at the water-limited sites. The impact of r_a on the LE residual error was found to be of the same magnitude as the influence of LST uncertainties in the semi-arid ecosystems as indicated by variable importance in projection (VIP) coefficients from partial least squares regression above unity. In contrast, our results for the mesic forest ecosystems indicated minor dependency on r_a for modelling LE (VIP < 0.4), which was due to a higher roughness length and lower LST resulting in the dominance of mechanically generated turbulence, thereby diminishing the importance of buoyancy production for the determination of r_a.

---

* Corresponding authors.
  E-mail addresses: ivonne.trebs@list.lu (I. Trebs), kaniska.mallick@gmail.com (K. Mallick).

1. Introduction

Aerodynamic resistance (hereafter r_a) expresses the efficiency of turbulent transport controlling the land-atmosphere (L-A) exchange of sensible heat (H) and water vapor between the source/sink height within a vegetation canopy and a reference height above the surface. It is the pivotal link that connects evapotranspiration (ET) with H through the surface energy balance (SEB) equation, and the estimation of r_a is central in thermal remote sensing of ET at local to regional scales (Bahir et al., 2017; Bhattarai et al., 2018; Kustas et al., 2007). Advanced understanding of L-A interactions is a prerequisite for accurate monitoring and predictions of Earth-system responses to drought, climate warming and surface drying. This is also one of the fundamental needs for developing effective mitigation strategies that minimize the socio-economic impacts of water scarcity caused by frequent droughts. Within this context, accurate estimation of the magnitude and variability of ET is critical for assessing the vegetation responses to drought and for developing knowledge of efficient water resources management (Anderson et al., 2011).

Contemporary SEB models use radiometric land surface temperature (LST) and meteorological variables to derive H while estimating ET (or its energy equivalent, the latent heat flux LE) as a residual SEB component (Chen and Liu, 2020). The r_a for momentum transfer (r_{aM}) is an unobserved variable, and its estimation is commonly based on the Monin-Obukhov similarity theory (MOST), which requires aerodynamic roughness parameters, friction velocity (u_*) and H as inputs (Foken, 2006). Major uncertainties of the MOST method are associated with the influence of complex/heterogeneous terrain, uncertainties in prescribing vegetation roughness and corrections for atmospheric stability (Holwerda et al., 2012; Sun et al., 2020; van Dijk et al., 2015; Zhou et al., 2012). Lee and Buban (2020) found that the Richardson number stability correction functions based on bulk meteorological variables yielded better agreement with field observations than using MOST relationships. These challenges are further exacerbated by the ambiguity in estimating the difference between r_{aM} and the r_a for heat transfer (r_{aH}), whereby complexity is added due to the inequality of LST and the aerodynamic temperature (T_0) (Paul et al., 2014).

LE is typically overestimated by the contemporary SEB models under dry conditions (e.g., Gokmen et al., 2012; Gokool et al., 2020; Morillas et al., 2013; Pardo et al., 2014; Seneviratne et al., 2010; van der Kwast et al., 2009). Although this overestimation tendency has been addressed by revisiting the soil resistance formulation (Kustas et al., 2016; Li et al., 2019) and integration of an environmental stress factor or NDVI scaling factor for model calibration (Gokmen et al., 2012; Gokool et al., 2020; Pardo et al., 2014), operating SEB models in water-scarce ecosystems may also be subject to errors in the determination of r_{aM} and r_{aH}. In these ecosystems, variations in H and LE are strongly determined by the feedback-response relationships between soil moisture availability and biophysical resistances (Cleverly et al., 2013; Jarvis and McNaughton, 1986; Raupach, 2001). Since the magnitude of LE is small compared to H, the performance of SEB models is expected to be highly sensitive to the uncertainties in r_a (Gokool et al., 2020; Mallick et al., 2016). While the biophysical impact of r_a on the LST response to vegetation changes and Earth greening was investigated recently (Chen et al., 2020; Liao et al., 2018; Winckler et al., 2019), and the influence of the inverse Stanton number (kB^{-1}) on SEB model performance has been discussed extensively (Boulet et al., 2012; Paul et al., 2014; Troufleau et al., 1997), the knowledge gap on the role of r_a for SEB model uncertainty has not yet been fully explored. Any attempt to advance the representation of L-A interactions within the SEB models is hindered due to the use of empirical functions to characterize the roughness and atmospheric stability components of r_a, which are generally not measurable at scales in which the remote sensing-based ET mapping is applied. Due to its fundamental importance in LST-based ET mapping and drought monitoring, r_a is a key variable that merits a detailed investigation to understand the extent of error propagation in ET estimates from different SEB models.

The scientific objective addressed by this study is to analyze the dependency on r_a of the uncertainty in predicted instantaneous LE using three structurally different SEB models that use dissimilar approaches to retrieve r_a. We hypothesize that r_a largely controls the predictive uncertainty of SEB models, and its influence on the errors of instantaneous LE retrievals is potentially comparable to the impact of LST. This hypothesis is tested by exploiting the remotely sensed LST information in SEB models that are validated with in-situ eddy covariance (EC) observations from a range of contrasting ecosystems with different aridity of the OzFlux network in Australia (Beringer et al., 2016; Mallick et al., 2018a).

Section 2 sets out the methodology that includes a brief description of the models, input variables and statistical analysis. Section 3 describes the data sources used in the study. The results are presented in Section 4, while the discussion and conclusion are elaborated in Section 5 and 6, respectively.

2. Methodology

2.1. SEB models for estimating ET

LST obtained from thermal infrared (TIR) remote sensing provides the key lower-boundary condition in SEB models for diagnostic estimates of LE and evaporative stress (Anderson et al., 2011; Chen and Liu, 2020). One-source SEB models treat the soil-vegetation complex as a single system, deriving lumped LE from the information of composite LST (Boegh et al., 2002; Su, 2002). Two-source SEB models treat the soil-vegetation complex independently and decompose LST into soil and vegetation temperatures whilst deriving the ET components (evaporation and transpiration) separately (Boulet et al., 2015; Kustas and Anderson, 2009). Both approaches are based on an appropriate expression of r_{aM} and r_{aH} for solving H, estimating LE as a residual in the SEB equation (Eq. (1)) (given net radiation (Rn) and soil heat flux (G) are known or estimated individually).

$$LE = Rn - G - H \ \left(\mathrm{W/m^2}\right) \tag{1}$$

The bulk formulation of H is based on the flux-gradient relationship:

$$H = \frac{\rho c_p (T_0 - T_a)}{r_{aH}} \ \left(\mathrm{W/m^2}\right) \tag{2}$$

where ρc_p is the volumetric heat capacity of air (J/K/m³), T_0 (K) is the aerodynamic temperature at the effective canopy source height at which energy fluxes arise and T_a (K) is the reference level air temperature. Despite substantial progress in global, regional and field scale ET mapping (Anderson et al., 2011; Bahir et al., 2017), implementation of SEB models is challenged by the uncertain specification of vegetation roughness and atmospheric stability variables for determining r_{aH} and also due to the empirical adjustments to accommodate for the inequalities between LST and T_0 (Paul et al., 2014). Calculation of r_{aH} requires addition of an external resistance (r_{ex}) to r_{aM}, which involves the kB^{-1} concept (Chen et al., 2019a, 2019b; Chen et al., 2013; Su, 2002):

$$r_{aH} = r_{aM} + r_{ex} \ (\mathrm{s/m}) \tag{3}$$

$$r_{ex} = \frac{1}{\kappa u_*} kB^{-1} \ (\mathrm{s/m}) \tag{4}$$

where κ is the von Kármán constant (=0.4) and u_* is the friction velocity (m/s). In Eq. (3), r_{aH} is greater than r_{aM}, i.e. momentum transport is more efficient than heat transport (Kustas et al., 2016). This implies that the source height for heat is lower than that for momentum, because heat is generated at the surface and its transfer is additionally controlled by molecular diffusion through the quasi-laminar sublayer (Verma, 1989). However, due to the use of LST instead of T_0 (Eq. (2)), kB^{-1} is not

Table 1

Overview of r_{aM} (r_{aH}) formulations used in three different SEB models. The symbols not mentioned in the main text are explained in the third column.

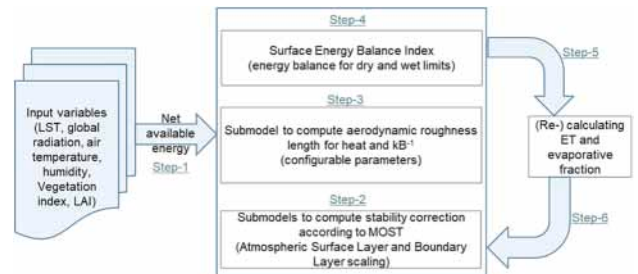| SEB model	Formulation of r_{aM} (r_{aH})	Symbols
SPARSE	$$r_{aM} = \frac{ln\left(\frac{z-d}{z_{0m}}\right)^2}{\kappa^2 u(1+R_{ib})^m}$$ m = 0.75 under unstable conditions and m = 2 under stable conditions	z: measurement level of wind speed (m) d: zero-plane-displacement height (m) z_{0m}: aerodynamic roughness length for momentum transfer (m) u: wind speed at measurement level (m/s) g: standard acceleration due to gravity (9.81 m/s^2) R_{ib}: Richardson number (Choudhury and Monteith, 1988)
SEBS	$$R_{ib} = \frac{5g(z-d)(T_0 - T_a)}{T_a u^2}$$ $$r_{aH} = \frac{1}{\kappa u_*}\left[ln\left(\frac{z-d}{z_{0h}}\right) - \psi_h\left(\frac{z-d}{L}\right) + \psi_h\left(\frac{z_{0h}}{L}\right)\right]$$ with $$z_{0h} = \frac{z_{0m}}{exp\left(kB^{-1}\right)}$$ $$L = \frac{\rho c_p u_*^3 \theta_v}{\kappa g H}$$	L: Monin-Obukhov length (m) z_{0h}: aerodynamic roughness lengths for heat transport (m) ψ_h: universal function for sensible heat (Brutsaert, 1992, 1999) θ_v: potential virtual temperature at the measurement level (K)
STIC	$$r_{aH} = \frac{\rho c_p\left[(T_0 - T_a) + \left(\frac{e_0 - e_a}{\gamma}\right)\right]}{\phi}$$ Estimation of T_0 is based on finding an analytical solution of a host of state equations. Estimation of e_0 is based on solving the saturation vapor pressure at the source/sink height and solving the vapor pressure deficit at the source/sink height of vegetation by combining Penman-Monteith and Shuttleworth-Wallace combination equations. Details are available in Mallick et al. (2016, 2018a).	e_0: vapor pressure at the source/sink height (hPa) γ: psychrometric constant (hPa K^{-1}) ϕ: net available energy (W/m^2)
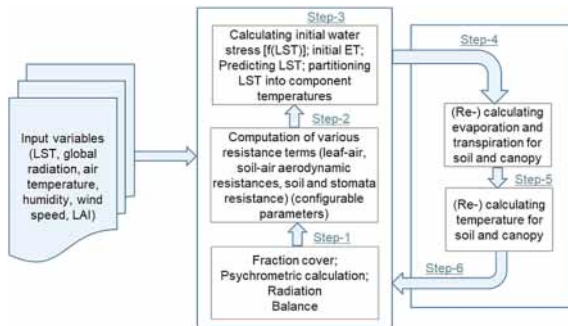
Fig. 1. Simplified flowchart of the SPARSE algorithm in retrieval mode. For a more detailed description see Boulet et al. (2015).

Fig. 2. Simplified flowchart of the SEBS algorithm. For a more detailed description see Su (2002).

related to its original theoretical background, but it has become a purely empirical fitting parameter called radiometric kB^{-1} (Paul et al., 2014).

Despite the important role of LST in estimating ET, SEB models also require highly accurate r_{aM} and r_{aH}, but their role in governing the errors of modelled LE has received little attention to date. The three models employed in this study substantially differ in their structure, and, particularly, in their approaches to calculate r_{aM} and r_{aH} (see Table 1).

2.1.1. SPARSE

A new two-source ET model, the Soil Plant Atmosphere and Remote Sensing Evapotranspiration (SPARSE) model (Boulet et al., 2015; Saadi et al., 2018) tends to overcome the challenges associated with the inequality between T_0 and LST (Fig. 1). SPARSE extends the original Two-Source Energy Balance (TSEB) model (Norman et al., 1995) in several aspects, notably by accounting for the effect of the vapor pressure deficit (VPD). It linearizes the full set of energy budget equations and is based on the r_{aM} expression of Choudhury and Monteith (1988) using measured wind speed, and the correction for atmospheric stability based on the bulk Richardson number (R_{ib}) that uses estimates of T_0 (Table 1). It constrains the surface energy budgets of the main heat and vapor sources in soil and vegetation with the remotely sensed LST to

retrieve instantaneous evaporation and transpiration rates. A layer (series) and a patch (parallel) version (Lhomme et al., 2012) of the model are available. SPARSE was operated in the retrieval mode where LST is an input (derived either from satellite observations or in-situ measurements in the thermal infrared domain). In its standard setup, SPARSE uses empirical relationships to derive roughness parameters from canopy height (h_c) ($z_{0m} = 0.13h_c$ and $d = 0.65h_c$) for dense vegetation. These were modified to $d = 0.6h_c$ for sites with sparse vegetation (Th. Foken, personal communication), for which z_{0m} was derived from EC data (see Table 3, Section 3.1) (Foken, 2017). The estimation of Rn in SPARSE is detailed in Boulet et al. (2015). Soil heat flux was calculated as a fraction of soil net radiation according to the time of day and ecosystem type. This approach showed comparable or even better results than the ones of e.g. Choudhury et al. (1987) or Su (2002) using LAI or fraction cover (F_c) as additional scaling variables. The required input data to run SPARSE are LST, emissivity, surface albedo, view zenith angle (vza), leaf area index (LAI), h_c, incoming solar radiation, wind speed, air temperature and relative humidity at a reference level.

To obtain consistent results and to understand the effects of r_a on LE uncertainties, simulations with the two other models (SEBS and STIC) were constrained using the net available energy (Φ) derived from SPARSE. This simplifies disentangling the influence of modelled Φ which impacts LE by residual (Eq. (1)).
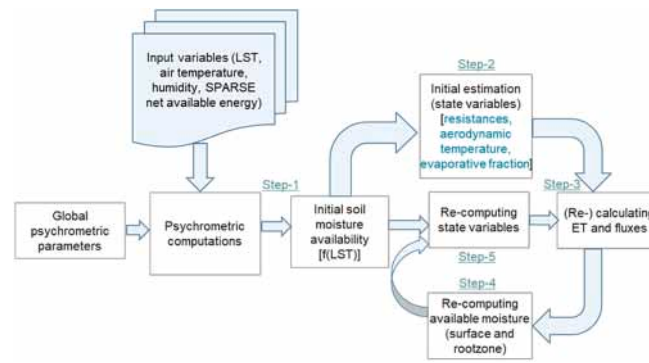
Fig. 3. Simplified flowchart of the STIC1.2 algorithm. For a more detailed description see Mallick et al. (2015).

2.1.2. SEBS

One-source models, such as the Surface Energy Balance System (SEBS) (Fig. 2) address the inequality between T_0 and LST by introducing r_{ex} and the kB^{-1} concept (Chen et al., 2013; Su, 2002). SEBS derives the SEB components by treating the soil-vegetation composite as a single unit (Su, 2002; Su et al., 2001). It estimates H for the driest and wettest boundary conditions (H_{dry}, H_{wet}). Based on H_{dry}, H_{wet} and actual H, relative evaporation (Λ_r) and evaporative fraction (Λ) are estimated by scaling the actual H with its dry and wet limits (details in Su, 2002). LE is derived through Λ and net available energy. Estimation of r_{aH} involves parameterization of the turbulent heat flux using MOST following an iteration procedure to derive u_*, L and H by implementing the stability correction functions (Brutsaert, 1992, 1999) (Table 1). Like most one-source models, SEBS is based on the estimation of the kB^{-1} factor. For this study, a revised model version including modifications presented in González-Dugo et al. (2020) and Chen et al. (2013) was used. Because the main objective of the paper is to explore model dependency on r_a, instead of using the canopy momentum transfer model (Massman and Weil, 1999), we used constant z_{0m} and d values (see Table 3, Section 3.1) to assign identical aerodynamic parameters for SPARSE and SEBS. The other required input data are comparable to those of SPARSE.

2.1.3. STIC

The Surface Temperature Initiated Closure (STIC, version 1.2) model is a one-source non-parametric ET model (Fig. 3) (Mallick et al., 2015; Mallick et al., 2014; Mallick et al., 2018a; Mallick et al., 2016). It was developed to circumvent the uncertainties associated with LST versus T_0 inequalities and MOST-r_a parameterizations for satellite-based ET mapping (Bhattarai et al., 2018). STIC is a one-dimensional physically based SEB model based on integrating LST observations into the Penman-Monteith energy balance equation and finding analytical solutions for r_{aH} (Table 1) and canopy-substrate resistance (r_c) that are independent of any empirical parameterizations. One of the fundamental assumptions in STIC is the first order dependence of r_{aH} and r_c on soil moisture through LST. By integrating LST with standard SEB theory, STIC formulates multiple state equations. These state equations are expressed as a function of those variables that are either directly available or deducible from remote sensing observations. Therefore, the equations can be solved algebraically to find analytical solutions of the resistances and T_0. Although most input variables for STIC are similar to those of SPARSE and SEBS, STIC does not require LAI and aerodynamic parameters (z_{0m} and d).

2.2. Retrieval of input variables

Although most of the required input variables were directly measured at the flux tower sites (Section 3), additional quantities were also needed for the model runs. The calculation of time-variant surface emissivity (ε) to retrieve in-situ LST estimates was performed following Jimenez-Munoz et al. (2006):

$$\varepsilon = \varepsilon_{vi}F_c + \varepsilon_{si}(1 - F_c) \tag{5}$$

where ε_{vi} and ε_{si} are band emissivity values for vegetation (0.99) and bare soil (0.96), respectively, and F_c is the fractional vegetation cover. The latter was derived according to:

$$F_c = 1 - e^{\left(\frac{-K \cdot LAI}{\cos(vza)}\right)} \tag{6}$$

where K is the attenuation coefficient of incoming radiation within the canopy (0.45), LAI is the leaf area index derived from MODIS LAI product (MCD15A2H) and vza is the MODIS view zenith angle.

The radiation balance was measured by pyranometer pairs (for shortwave components) and pyrgeometer pairs (for longwave components) mounted on the EC towers. Estimates of surface albedo to model net radiation were derived from in-situ upwelling and downwelling short wave radiation measurements. In-situ LST was computed from measured upwelling and downwelling longwave radiation covering the same spectral range using the Stefan-Boltzmann law (e.g. Chen et al., 2017):

$$LST_{in-situ} = \left(\frac{L\uparrow - (1-\varepsilon)L\downarrow}{\varepsilon\sigma}\right)^{\frac{1}{4}} \tag{7}$$

where $L\uparrow$ (W/m²) is the upwelling longwave radiation, $L\downarrow$ (W/m²) is the downwelling longwave radiation, ε is the surface emissivity, $LST_{in-situ}$ (K) is the surface temperature and σ (W/m²/K⁴) is the Stefan Boltzmann constant.

2.3. Statistical analysis

The following statistical metrics were used to evaluate the model performances for instantaneous LE at satellite overpass time:

Root mean Square Error (W/m^2) :

$$RMSE = \sqrt{\frac{1}{n}\sum_{i=1}^{n}\left(LE_{mod} - LE_{obs}\right)^2} \quad (8)$$

Mean Bias Error (W/m^2) :

$$MBE = \frac{1}{n}\sum_{i=1}^{n}\left(LE_{mod} - LE_{obs}\right) \quad (9)$$

Mean Absolute Percentage Error $(\%)$:

$$MAPE = \frac{1}{n}\sum_{i=1}^{n}\left|\frac{LE_{obs} - LE_{mod}}{LE_{obs}}\right| \quad (10)$$

Kling Gupta Efficiency :

$$KGE = 1 - \sqrt{(r-1)^2 + \left(\frac{\sigma_{mod}}{\sigma_{obs}} - 1\right)^2 + \left(\frac{\mu_{mod}}{\mu_{obs}} - 1\right)^2} \quad (11)$$

where the subscript 'mod' refers to modelled values and the subscript 'obs' refers to the observed values; r denotes the linear correlation between observations and simulations, σ denotes the standard deviation, and μ represents the mean. KGE = 1 indicates perfect agreement between simulations and observations, while a negative KGE indicates unsatisfactory model performance (for details see Knoben et al., 2019).

Furthermore, Partial Least Squares Regression (PLSR) was employed to identify fundamental relationships between the residual *LE* error and a host of variables. These were intermediate model variables (e.g., Φ, r_{aM},

r_{aH} and kB^{-1}) as well as model input variables (e.g. LST). Regressions were made using the SIMPLS algorithm, which calculates PLS factors directly as linear combinations of the original variables (de Jong, 1993) after all variables were normalized. In order to quantify and present the relationship between the variables and the *LE* residual, we derived the Variable Importance in Projection (VIP) scores based on the normalized PLS weights, scores and loadings according to Chong and Jun (2005).

3. Datasets

3.1. In-situ datasets

This study is based on high-quality EC and meteorological datasets for both model input and model evaluation from the regional Australian flux tower network OzFlux (http://data.ozflux.org.au/portal/home.jspx) that is funded by the National Collaborative Infrastructure Strategy (NCRIS) though the Terrestrial Ecosystem Research Network (TERN) platform (https://www.tern.org.au/) (Beringer et al., 2016). The three models were operated for the years 2011–2019 for a selection of nine OzFlux sites all over Australia including a wide range of ecosystem types, climates and aridity (Table 2). We used Level 3 datasets that were post-processed, corrected, but not gap-filled (Isaac et al., 2017).

Australia is a predominantly arid and semi-arid continent with substantial fluctuations in precipitation and primary production (Cleverly et al., 2016). In contrast, there are some mountainous rainforest locations where annual average precipitation exceeds 4000 mm (Glenn et al., 2011). The ecosystems in the Northern Territory (NT) of Australia (ASM, Stp, Dry, DaS, Table 2) are characterized by distinct wet and dry

Table 2
Summary showing general characteristics of the measurement sites of the Australian flux tower network used in this study. Model simulations were made for the period 2011–2019 (except GWW 2013–2019).

Aridity	Site	Lat/Lon	Ta (min-max) (°C)	P (±σ) (mm)	Budyko aridity index mean (range)	World ecoregion
arid	Alice Springs Mulga (ASM)	−22.2828/133.2493	−0.8–43.4	302 (61)	31 (6–133)	Deserts and xeric shrublands
	Calperum (Cpr)	−34.0027/140.5877	−3.8–47.7	207 (66)	21 (8–40)	Mediterranean woodlands
	Great Western Woodlands (GWW)	−30.1913/120.6541	1.9–45.8	283 (52)	11 (5–22)	Mediterranean woodlands
semi-arid	Gingin (Gin)	−31.3764/115.7139	−0.14–43.3	560 (44)	8 (4–22)	Mediterranean woodlands
	Sturt Plains (Stp)	−17.1507/133.3502	4.4–45.4	581 (48)	7 (2–26)	Tropical grasslands
	Dry River (Dry)	−15.2588/132.3706	5.9–42.0	708 (43)	6 (2–12)	Tropical savannas
mesic	Wombat (Wom)	−37.4222/144.0944	−0.9–37.3	719 (46)	4 (1–6)	Temperate broadleaf forest
	Daly Uncleared (DaS)	−14.1592/131.3881	8.9–39.6	1116 (34)	4 (3–10)	Tropical savannas
	Tumbarumba (Tum)	−35.6566/148.1517	−5.5–33.7	914 (46)	1.6 (0.8–2)	Temperate broadleaf and mixed forest

Table 3
Summary showing specific characteristics of the measurement sites of the Australian flux tower network used in this study. The value of d was set to $^2/_3 h_c$ for dense vegetation and to $0.6 h_c$ for sparse vegetation (Th. Foken, personal communication). The values for z_{0m} were set to $0.13 h_c$ for dense vegetation and calculated from Eqs. 2.67 and 3.1 in Foken (2017) for sparse vegetation. Mean values of the SEB closure were calculated at MODIS Terra and Aqua overpass times (see Section 3.2) for 2011–2019.

Site	canopy height (m)	LAI range (m²/m²)	z_{0m} (m)	d (m)	SEB closure (%)
Alice Springs (ASM)	6.5	0.16–0.85	1.0	3.9	82
Calperum (Cpr)	3.0	0.17–0.66	0.21	1.8	93
Great Western Woodlands (GWW)	18.0	0.29–0.49	0.2	10.8	77
Gingin (Gin)	6.8	0.58–1.27	0.7	4.08	84
Sturt Plains (Stp)	0.5	0.15–1.35	0.065	0.325	92
Dry River (Dry)	12.3	0.7–2.0	1.2	7.38	78
Wombat (Wom)	23.0	2.2–4.9	2.5	13.8	82
Daly Uncleared (DaS)	16.4	0.66–2.5	2.0	9.84	91
Tumbarumba (Tum)	40.0	1.0–3.4	5.2	26.0	74

seasons and highly seasonal rainfall driven by monsoonal weather systems (Bowman et al., 2010). The sites located in the southern, south-eastern and south-western part of Australia (Cpr, GWW, Gin, Wom, Tum, Table 2) are affected by extra-tropical weather patterns and the wet season is in the winter (Jun-Aug) while the dry season is in the summer (Dec-Feb) (except at GWW, where rainfall is summer dominant for the past ten years).

The arid ecosystems toward central Australia are subject to very low rainfall amounts mainly occurring as occasional precipitation (*P*) pulses, resulting in a very low top-soil water content (SWC < 20%) most of the time (Mallick et al., 2018a). They are characterized by strong surface heterogeneity and extremely low soil moisture coupled with high *VPD*.

By adopting the aridity classification as reported in Mallick et al. (2018a), we defined that sites with a mean Budyko aridity index (*BAI* = ET_{pot}/P) greater than 10 are strongly water-limited (arid), which include ASM, Cpr, and GWW. The sites Gin, Stp, and Dry are considered as semi-arid (mean BAI = 5–10). Sites with a mean BAI < 5 are considered as energy-limited (mesic), i.e. Wom, DaS and Tum.

For model simulations, the half-hourly or hourly (for Tum only) in-situ data (including in-situ-*LST*) were interpolated to the timestamp of satellite overpass (see Section 3.2). Table 3 shows detailed characteristics of the measurement sites that includes LAI, estimated aerodynamic roughness parameters and mean values of the SEB closure, respectively. The statistical intercomparison of SEB model results against flux observations were performed by forcing the Bowen Ratio Energy Balance (BREB) closure adding energy to *LE* and *H* in proportion to the measured Bowen ratio (Mauder et al., 2020; Twine et al., 2000).

3.2. Remote sensing datasets

LST is a key input variable for the three models employed in this study. The Moderate Resolution Imaging Spectroradiometer (MODIS), an instrument onboard NASA's Terra and Aqua polar-orbiting satellite platforms, provides daily *LST* at a spatial resolution of 1 km. Daily observations of MODIS Terra and Aqua *LST* (MOD11A1, MYD11A1, v006) were acquired from the Land Processes Distributed Active Archive Centre (LPDAAC) for the corresponding tower pixels according to the latitude and longitude provided in Table 2. This resulted in *LST*, emissivity, and corresponding *vza* values coincident with the MODIS Terra and Aqua overpass timestamp for the period 2011–2019. Data for *vza* > 40° and cloud contaminated *LSTs* were excluded from the analysis.

Furthermore, the MODIS Terra-Aqua combined 4-day LAI (MCD15A2Hv006) product with a spatial resolution of 500 m was used

as model input (Table 3) for estimating F_c (Eq. (6)) and calculating the kB^{-1} factor in SEBS (Chen et al., 2013; Su, 2002); the amount of net radiation intercepted by the canopy and the leaf-air aerodynamic resistance in SPARSE (Boulet et al., 2015). The extracted LAI values from the MCD15A2Hv006 product for each site (Table 3) were cross-checked with in-situ LAI measurements when available.

4. Results

The complete statistical results of modelled *H* and *LE* for all sites are presented in the Appendix (Tables A1-A6). For SPARSE, only results of the parallel resistance version of the model in the retrieval mode are shown, which is justified by the ecosystem types (often sparse vegetation). Simulated *LE* of the parallel model version compared better to the observations than that of the series model version for most of the sites. In some cases, model convergence was not achieved mainly due to high *LST* values, and these data were omitted from the analysis (see Tables A1 and A2).

For SEBS, in case the dry limits were reached (Mallick et al., 2018b), zero values of *LE* were rejected from further analysis (see Tables A3, A4). This is done to adapt with the structural uncertainties of SEBS in estimating relative evaporation (Λ_r) under the dry limits. In SEBS, Λ_r is estimated by scaling the actual *H* with *H* for the driest (H_{dry}) and wettest (H_{wet}) conditions [$\Lambda_r = 1 - (H - H_{wet})/(H_{dry} - H_{wet})$; and $H_{dry} = Rn - G$] (Su, 2002). Any condition that produces $H = H_{dry}$, would tend to simulate $\Lambda_r = 0$, and *LE* will be consequently zero (Mallick et al., 2018b).

For STIC, no such rejection criteria are needed because of the structural characteristics of the model; and examples of iterative stabilization of STIC in different ecosystems are shown in previous studies (Mallick et al., 2015, 2016; Bhattarai et al., 2018).

In Section 4.1, the statistical results of the individual models are shown for *H* and *LE* using MODIS and in-situ *LST* as input. Sections 4.2–4.4 focus on the model results obtained using MODIS *LST* (Terra and Aqua) as input.

4.1. Model performance and intercomparison across sites with different aridity

For the SPARSE model, simulations using MODIS *LST* produced lower RMSE in instantaneous *H* and *LE* as compared to using in-situ *LST* at most of the sites (except for mesic ecosystems) (Fig. 4a,b). While the instantaneous *H* and *LE* from SPARSE showed lowest RMSE for the mesic sites (68–105 W/m²), the RMSE for arid and semi-arid sites was
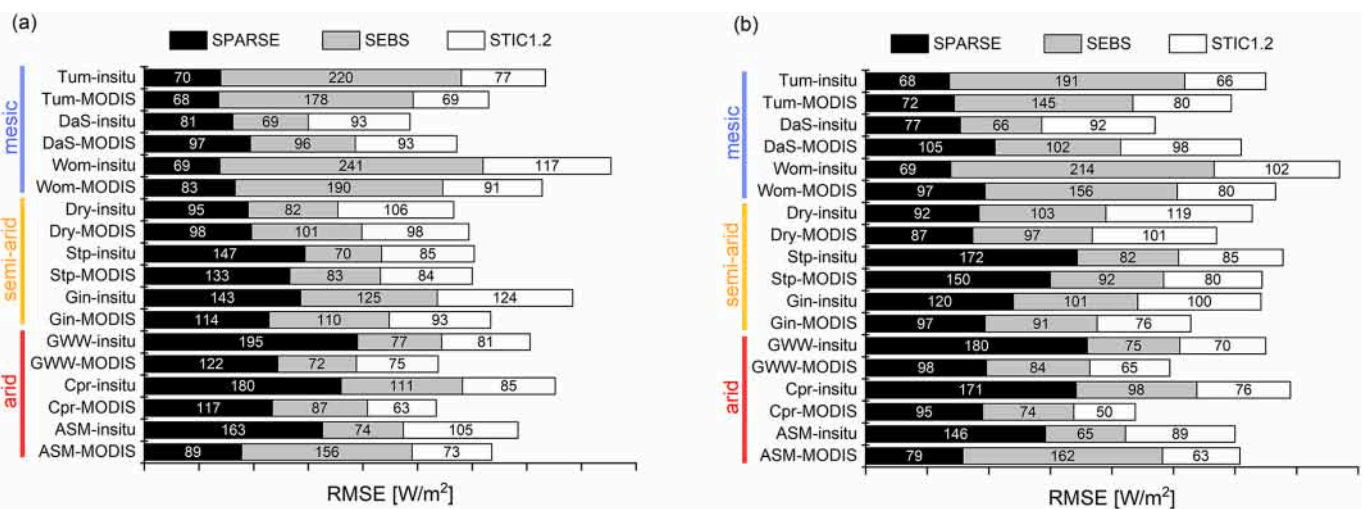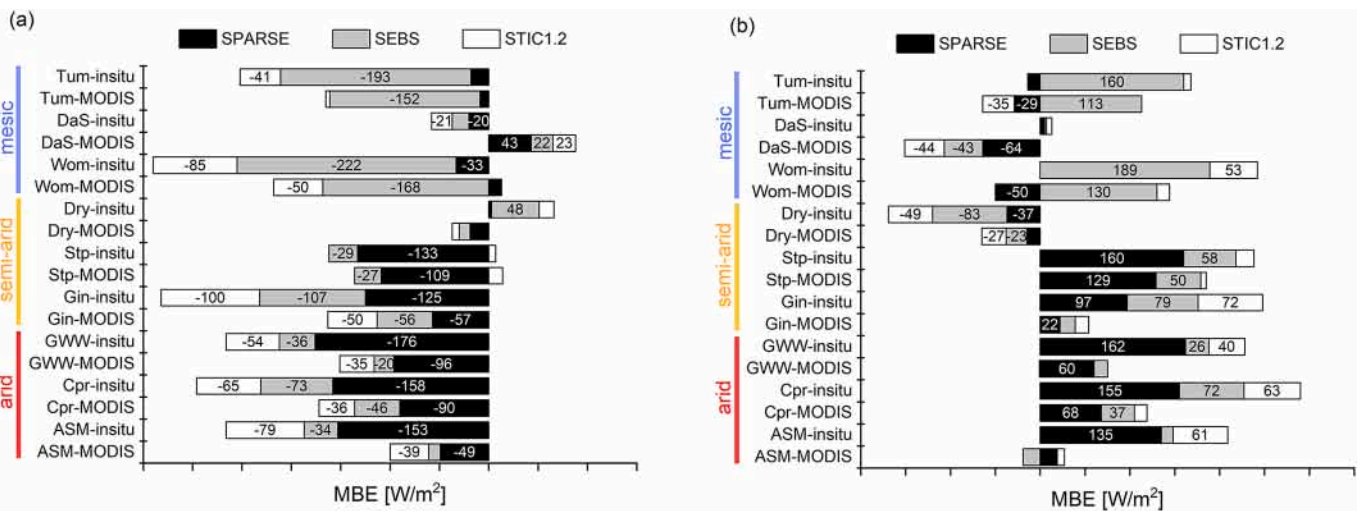

Fig. 4. Root Mean Square Error (RMSE) of the SPARSE (parallel version, retrieval mode), SEBS and STIC models for the instantaneous (a) *H* and (b) *LE* retrievals at satellite overpass times (MODIS Aqua and Terra) for nine sites of contrasting aridity in Australia using MODIS *LST* and in-situ *LST* as input. (For interpretation of the references to color in this figure legend, the reader is referred to the web version of this article.)
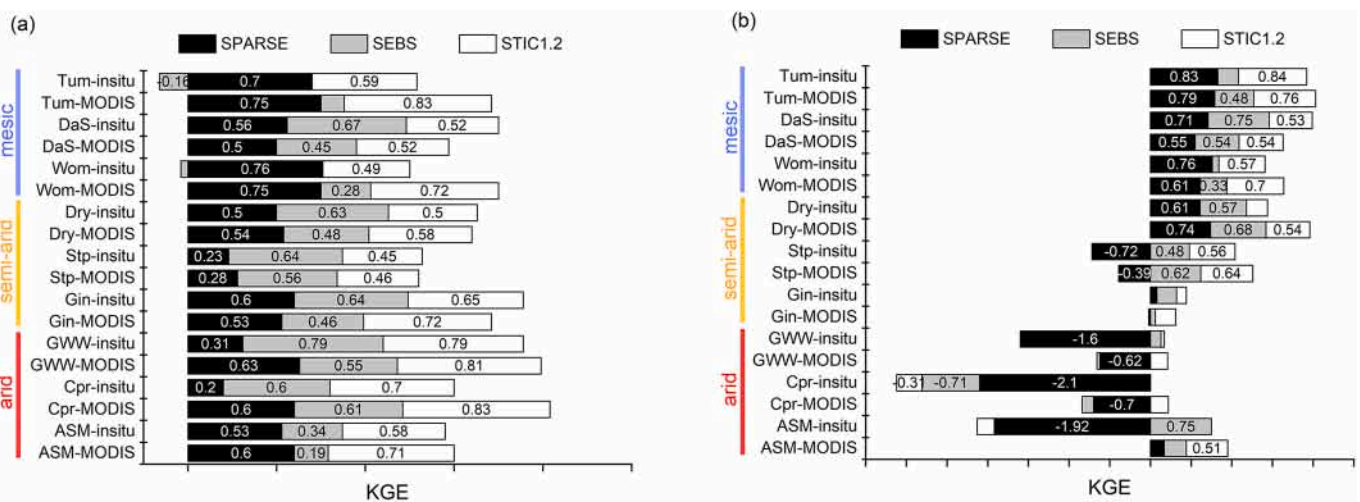
Fig. 5. Mean Bias Error (MBE) of SPARSE (parallel version, retrieval mode), SEBS and STIC models for instantaneous (a) *H* and (b) *LE* retrievals at satellite overpass times (MODIS Aqua and Terra) for nine sites of contrasting aridity in Australia using MODIS *LST* and in-situ *LST* as input. (For interpretation of the references to color in this figure legend, the reader is referred to the web version of this article.)

substantially higher (up to 195 W/m^2 for *H* and 180 W/m^2 for *LE*), particularly when in-situ *LST* was used as input. The highest RMSE was found for the tropical grassland (Stp) and for one of the Mediterranean woodlands sites (GWW). The RMSE of SEBS exceeded that of SPARSE for all mesic sites (69–241 W/m^2 for *H* and 66–214 W/m^2 for *LE*), while the RMSE of SEBS was lower than of SPARSE for arid and semi-arid sites, particularly when in-situ *LST* was used as model input (Fig. 4a,b). Instantaneous *H* and *LE* from STIC simulations resulted in lowest RMSE for the arid sites (63–105 W/m^2 for *H* and 50–89 W/m^2 for *LE*) (Fig. 4a, b). The highest RMSE values (> 90 W/m^2) from STIC for both *H* and *LE* were found for the savanna sites (Dry and DaS) as well as for Gin and Wom. Similar to SPARSE, the magnitudes of the RMSE from STIC were higher with in-situ *LST* for the majority of the sites. Overall, the RMSE was lower for STIC compared to the other two models and the magnitude of the RMSE for *H* and *LE* was comparable for all models.

Fig. 5 shows a significant underestimation (overestimation) of instantaneous *H* (*LE*) by SPARSE for the arid (ASM, Cpr, GWW) and semi-arid sites (Gin and Stp, except Dry) as revealed by high negative MBE values (−49 to −176 W/m^2) for *H* (Fig. 5a) and high positive MBE values (22 to 162 W/m^2) for *LE* (Fig. 5b). This underestimation

(overestimation) persisted for sites with both sparse and dense vegetation (Stp) and is more pronounced when in-situ *LST* was used to simulate *H* and *LE*. In contrast, SPARSE slightly underestimated *H* and *LE* for most of the mesic sites (MBE values between −64 and − 20 W/m^2) and model performance for *LE* improved with in-situ *LST* (MBE between −14 and 5 W/m^2). The *H* and *LE* bias from SEBS simulations (Fig. 5a,b) was not only dependent on aridity but also on the ecosystem type. On average, SEBS underestimated (overestimated) *H* (*LE*) for all sites except savanna ecosystems (Dry, DaS), where consistent overestimation of *H* and underestimation of *LE* was found (MBE of −23 to −83 W/m^2) (Fig. 5b). In contrast to SPARSE, SEBS substantially underestimated *H* and overestimated *LE* for mesic forest sites (Wom, Tum), which was more significant when in-situ *LST* was used as input (see Fig. 5a,b). Instantaneous *H* and *LE* from STIC revealed negative bias for *H* (−35 to −100 W/m^2) and positive bias for *LE* (6–72 W/m^2) for the arid and semi-arid ecosystems (except Dry), and a negative bias was found for both *H* and *LE* at the mesic ecosystems (MBE values between −21 and − 85 W/m^2) (Fig. 5a,b). The results of STIC for the two savanna sites (Dry and DaS) were comparable to those of the other two models (negative bias for *LE*). The overall performance of STIC was comparable to SPARSE, although

Fig. 6. Kling-Gupta efficiency (KGE) of SPARSE (parallel version, retrieval mode), SEBS and STIC models for instantaneous (a) *H* and (b) *LE* retrievals at satellite overpass times (MODIS Aqua and Terra) for nine sites of contrasting aridity in Australia using MODIS *LST* and in-situ *LST* as input. (For interpretation of the references to color in this figure legend, the reader is referred to the web version of this article.)
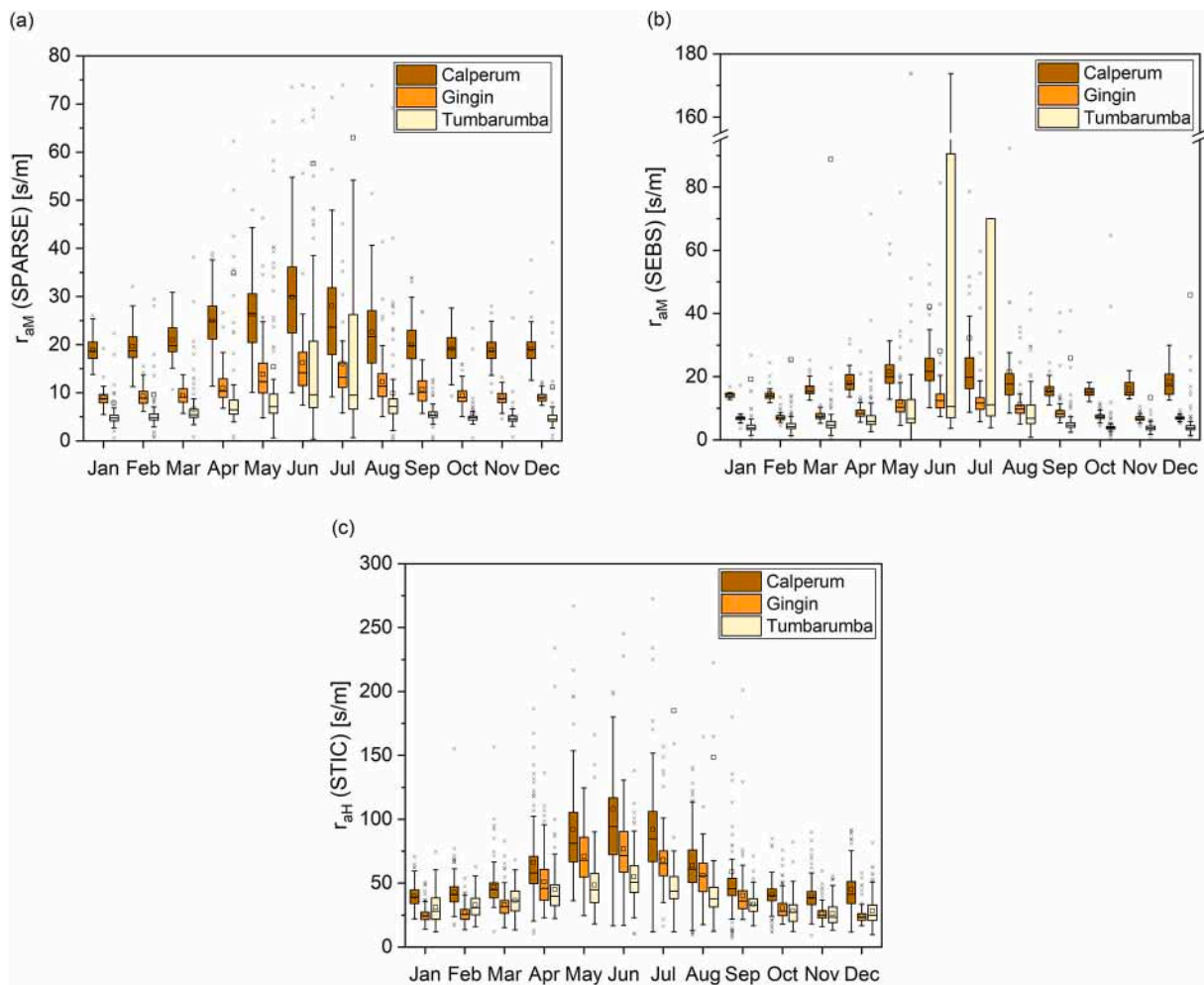
Fig. 7. Box-and-whisker plots showing seasonal variations of (a) r_{aM} simulated with the parallel version of the SPARSE model, (b) r_{aM} simulated with the SEBS model and (c) r_{aH} simulated with the STIC model using MODIS *LST* as input for three sites (z = 10 m (Cpr), z = 15 m (Gin), z = 70 m (Tum)) of contrasting aridity in Australia. Note the different ranges of y-axis.

the mean bias for STIC was lower for arid and semi-arid sites but higher for the mesic forest sites.

KGE statistics for *H* and *LE* showed comparable values for SPARSE and STIC (KGE > 0.5) that exceeded those of SEBS for the mesic sites (Fig. 6a,b). All KGE values were positive for *H* for the arid and semi-arid sites (Fig. 6a), while most values were negative for *LE* (Fig. 6b), which can be explained by the different magnitudes of *H* and *LE* at these sites (see Section 4.3). As the magnitude of *H* is large compared to *LE* under water-limited conditions, a small relative model error in *H* will propagate into a large relative error in *LE* (Payero et al., 2006) (see also MAPE values in Tables A1-A6). Although SPARSE results indicated positive KGE values for *H* (>0.2) (Fig. 6a), very low and negative KGE (Fig. 6b) were found for *LE* at most of the arid and semi-arid sites. The KGE of SEBS for *H* (*LE*) in the mesic sites varied between −0.16 and 0.67 (0.08 and 0.75). For the semi-arid sites, instantaneous *H* (*LE*) by SEBS was simulated with moderate accuracy (KGE > 0.45 (0.3)) and no major improvement in *LE* was found with in-situ *LST*. STIC revealed positive KGE values (>0.45) for *H* at all sites, and for *LE* positive KGE values were also found at nearly all sites with MODIS *LST*, being highest for the mesic sites (0.53–0.84).

In general, the overestimation of *LE* coincided with a comparable underestimation of *H* suggesting that the impact of *Φ* obtained with SPARSE on the *LE* model bias was of minor importance. The overall performance of the three models to estimate instantaneous *LE* was substantially improved for sites with lower aridity, as indicated by KGE,

RMSE, MBE, MAPE and R^2 values (Tables A1-A6) (except SEBS statistics for Wom and Tum). Moreover, forcing the models with in-situ *LST* did not yield any substantial improvement in the model performances at arid and semi-arid sites.
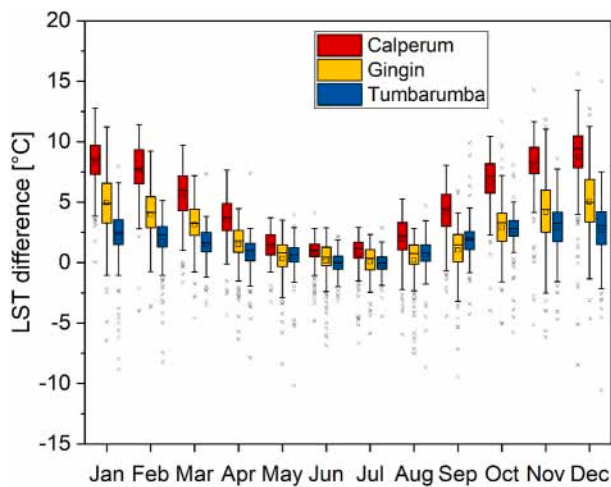
4.2. Seasonal variations

Results in Sections 4.2–4.4 focus on three sites in south, southwestern, and southeastern Australia, namely Calperum (Cpr), Gingin (Gin) and Tumbarumba (Tum), representing arid (Cpr) to semi-arid (Gin) and mesic (Tum) conditions.

4.2.1. Seasonal variations of r_{aM} and r_{aH}

The simulation of r_{aM} by SPARSE (Fig. 7a) showed an interquartile range (IQR) between 4 and 36 s/m and revealed a distinct difference in magnitude by a factor of two to three across sites, particularly during the dry season (Oct-Dec and Jan-Mar). The highest r_{aM} was found at Cpr as compared to the other sites, except during the wet season (Jun-Jul) when the difference between sites was less pronounced (Fig. 7a). Moreover, a strong inter-annual variation was found for all three sites. The largest values of r_{aM} were simulated during the wet season.

To gain more insight into the role of momentum transfer for SEBS, r_{aM} was calculated from r_{aH} (Table 1) according to Eqs. (3) and (4). Simulated r_{aM} by SEBS were lower than the r_{aM} of SPARSE, except during the wet season at Tum (Fig. 7b). SEBS r_{aM} exhibited an IQR between 14

Fig. 8. Box-and-whisker plots showing seasonal variations of the difference between MODIS *LST* and in-situ *LST* (*ΔLST*) for three sites of contrasting aridity in Australia. MODIS Terra and Aqua *LST* are combined in the analysis. (For interpretation of the references to color in this figure legend, the reader is referred to the web version of this article.)

and 25 s/m for Cpr and between 6 and 14 s/m for Gin, with a marked seasonal variation. However, r_{aM} featured a stronger seasonality at Tum, with values mainly ranging between 3 and 90 s/m (IQR). Extremely high values were simulated for June and July (wet season) (Fig. 7b), when periods of a highly stable boundary layer under cloudy and misty conditions occur frequently.

As STIC derives an analytical solution of r_{aH} (Mallick et al., 2015, 2018a), the nature of r_{aH} simulated by STIC is different to that of SEBS (Table 1) and the retrieval of r_{aM} is not straightforward in STIC. Furthermore, the r_{aH} of STIC is not influenced by corrections involving the kB^{-1} factor because STIC directly computes the aerodynamic temperature (Mallick et al., 2016). STIC r_{aH} (Fig. 7c) also indicated substantial seasonality with an IQR between 20 and 120 s/m. Although the seasonal pattern of STIC r_{aH} is comparable to SPARSE, across site variation in simulated r_{aH} is lower for STIC as compared to r_{aM} of the other two models. The highest and lowest r_{aH} values are estimated for Cal and Tum, respectively.

4.2.2. Seasonal variations of the LST difference

The *LST* difference (*ΔLST*) (= MODIS *LST* − in-situ *LST*) is used as a proxy for the potential bias in MODIS *LST*. The relationship of *ΔLST* to the *LE* residual error is compared to that of r_{aM} (r_{aH}) in the following sections of the paper.

The seasonal variation of *ΔLST* (Fig. 8) showed positive median *ΔLST*
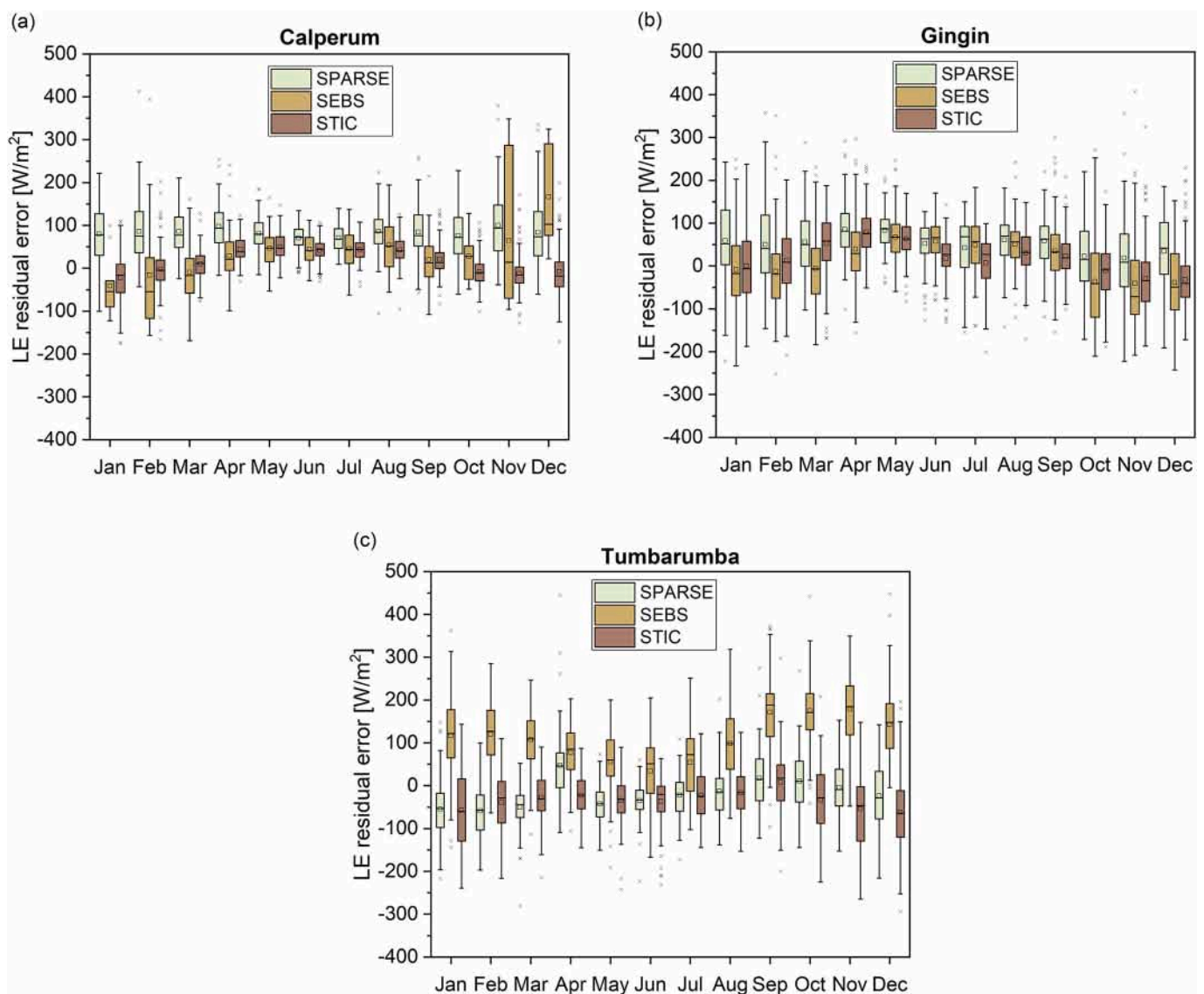
Fig. 9. Box-and-whisker plots showing seasonal variations of the *LE* residual error (difference between modelled and observed *LE*) for SPARSE (parallel version), SEBS and STIC using MODIS *LST* as input at three sites of contrasting aridity in Australia (a) Calperum, (b) Gingin and (c) Tumbarumba.
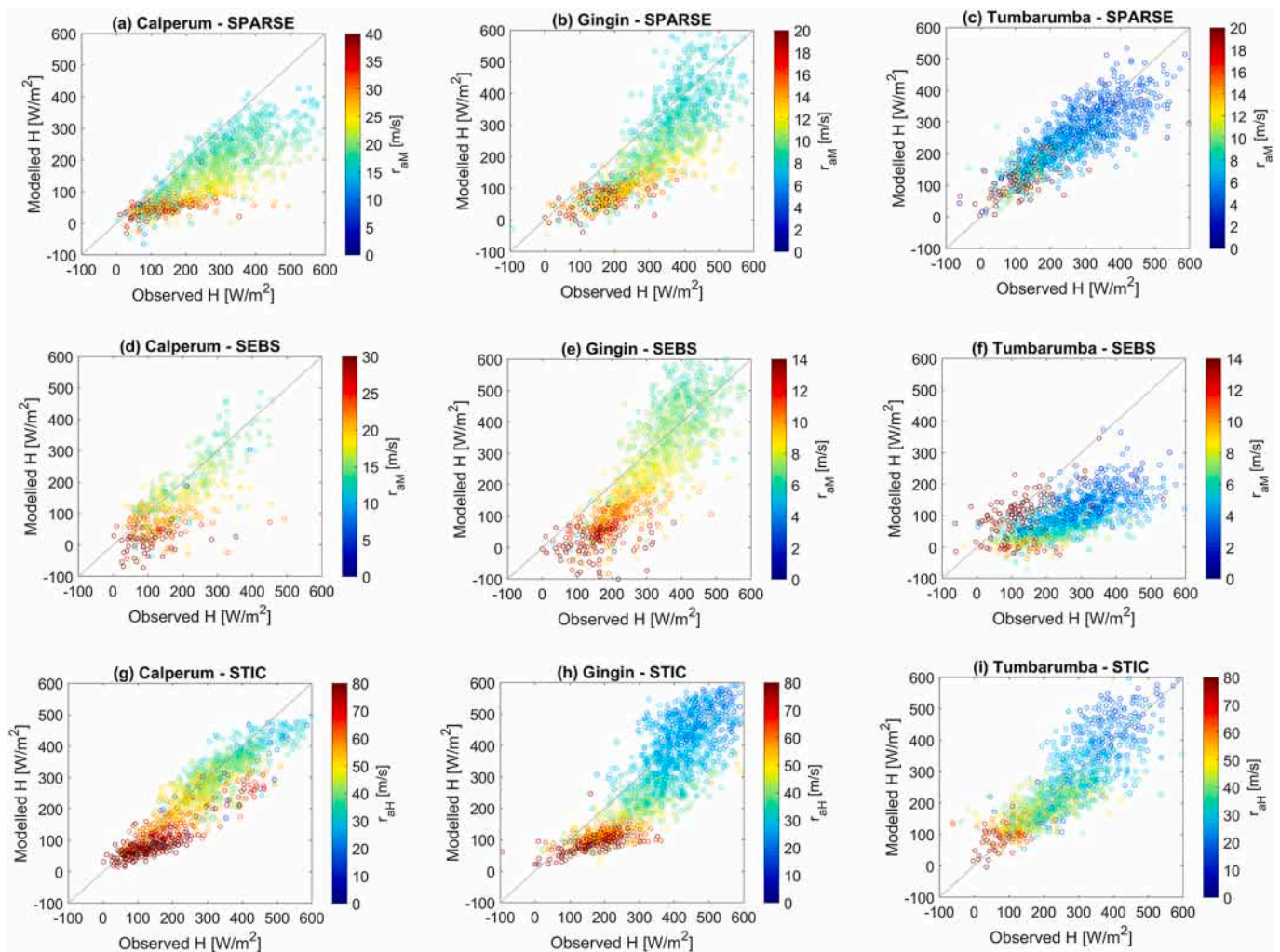
Fig. 10. Scatter plots of modelled *H* versus observed *H* color-coded with r_{aM} for SPARSE (a-c), SEBS (d-f) and r_{aH} for STIC (g-i) for the representative arid (Cpr), semi-arid (Gin), and mesic (Tum) sites using MODIS *LST* as input to simulate *H* with the three models. Regression statistics are presented in Tables A1, A3 and A5.

(1–10 °C), indicating MODIS *LST* to be higher than the in-situ values across all sites. This exceedance was most pronounced and had the largest seasonality for the arid site (Cpr) and declined with decreasing aridity (Gin and Tum, Table 2). The differences scaled with air temperature for each site (not shown for brevity) and were largest for the summer dry season (often > +5 °C at Cpr and Gin), when soil moisture was extremely low (SWC < 5%). Differences were close to zero at Gin and Tum during the winter wet season (mainly June to August), when frequent precipitation causes increased soil moisture and when air temperature is at a minimum. In-situ *LST* exceeded MODIS *LST* only occasionally, mainly during the winter wet season. The lower *ΔLST* during the wet season coincided with high r_{aM} and r_{aH} (see Fig. 7).

4.2.3. Seasonal variations of the LE residual error

The seasonal variation of the *LE* residual error revealed lowest values (median within −40 and 75 W/m^2) and the lowest IQR (−75 to 100 W/m^2) during the wet season for all three contrasting sites and all three models (Fig. 9a-c). As indicated by a large IQR, the variation of the *LE* residual error was highest during the dry season, ranging between 280 W/m^2 for SEBS at Cpr and − 140 W/m^2 for STIC at Tum. In general, the one-source models SEBS and STIC revealed the tendency to overestimate *LE* during the wet season and underestimate *LE* during the dry season at the water-limited sites (Cpr and Gin) (Fig. 9a,b). In contrast, SPARSE showed a consistent overestimation tendency of *LE* in nearly all months at Cpr and Gin, while in Tum the median residual error was often close to

zero (Fig. 9c). STIC mainly underestimated *LE* in Tum during the dry season (IQR −140 to 25 W/m^2), whereas SEBS showed a substantially large positive *LE* residual (IQR 25 to 230 W/m^2). Overall, for this mesic forest site, the largest variation amongst model results was found.

To summarize, turbulent transfer was lowest at the arid woodland site (Cpr) and highest at the mesic forest site (Tum), which is partly attributed to the different measurement heights (Fig. 7). Figs. 7 and 8 reveal that a high *ΔLST* coincided with low r_{aM} and r_{aH} during the dry season. The low or partly negative *ΔLST* during the wet season coincided with an overestimation of *LE* at water-limited sites (Fig. 9).

4.3. Dependency of the H and LE residual errors on r_{aM} (r_{aH}) and LST

Results for SPARSE in Fig. 10a,b and Fig. 11a,b indicate that underestimation of *H* and overestimation of *LE* is related to the magnitude of r_{aM} for the arid and semi-arid sites (Cpr and Gin). Underestimation (overestimation) of *H* (*LE*) predominantly occurred at high r_{aM} (i.e., low wind speed), while a good agreement between modelled and observed *H* (*LE*) or a slight overestimation (underestimation) was observed for low r_{aM} (i.e., high wind speed). This is indicated by values with high r_{aM} falling below (above) the 1:1 line and those with low r_{aM} falling close to or along the line in Fig. 10a,b and Fig. 11a,b. This dependency was not visible in the mesic forest site (Tum), where no systematic over/underestimation was found (Fig. 10c, 11c).

The results of SEBS and STIC for the water-limited sites (Cal and Gin)
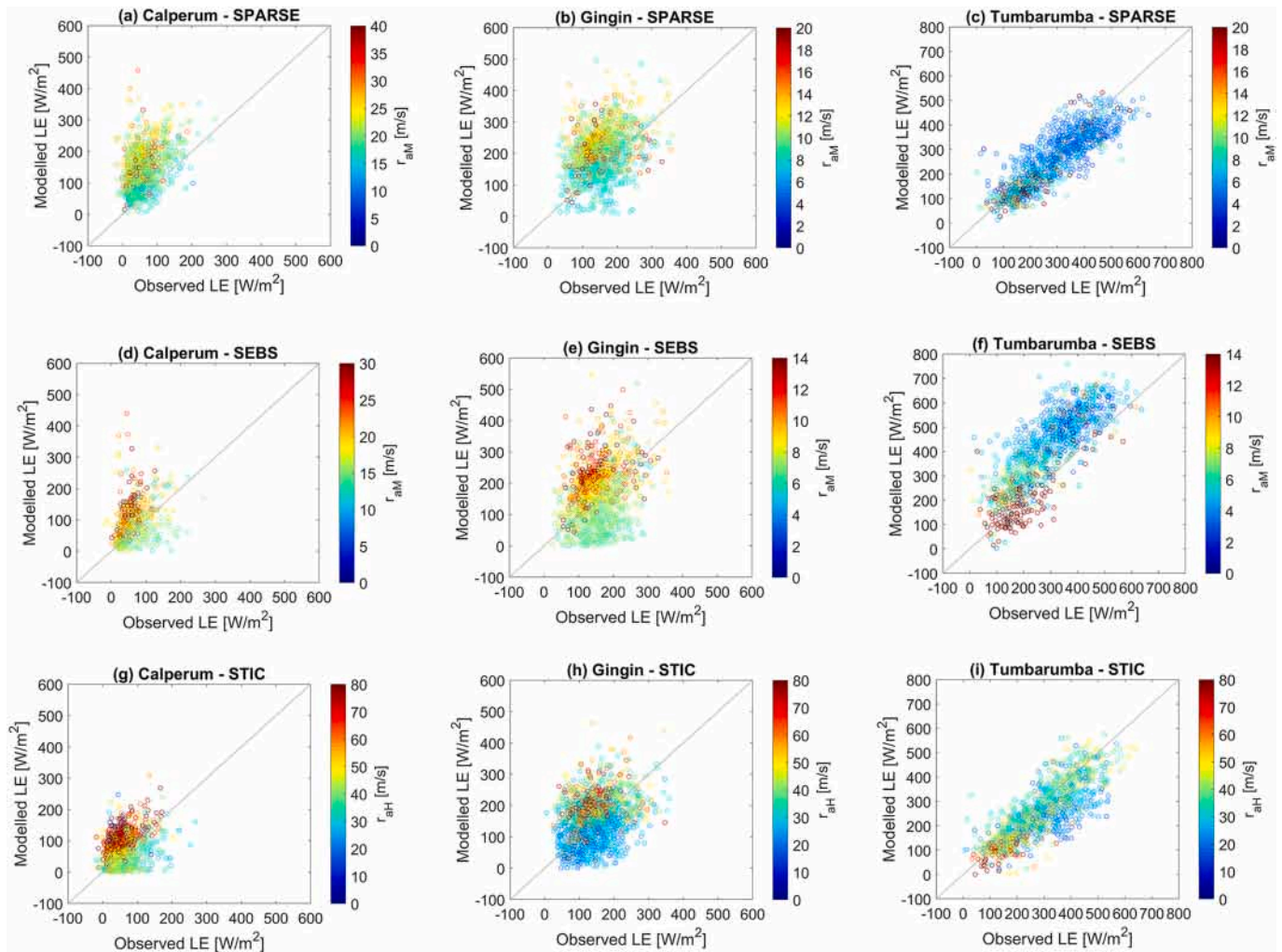
Fig. 11. Scatter plots of modelled *LE* versus observed *LE* color-coded with r_{aM} for SPARSE (a-c), SEBS (d-f) and r_{aH} for STIC (g-i) for the representative arid (Cpr), semi-arid (Gin), and mesic (Tum) sites using MODIS *LST* as input to simulate *LE* with the three models. Regression statistics are presented in Tables A2, A4 and A6.

revealed comparable patterns as found for SPARSE (Figs. 10d,e,g,h and 11d,e,g,h), although the *LE* underestimation for low r_{aM} and r_{aH} was more pronounced compared to SPARSE. At Tum, a minor dependency on r_{aM} was evident for SEBS (Figs. 10f and 11f), in which predominant underestimation (overestimation) of *H* (*LE*) was found at low r_{aM} (i.e., high wind speed), in contrast to the pattern at the water-limited sites. This suggests that the substantial *LE* overestimation by SEBS at Tum is not caused by uncertainties in r_{aM}. For STIC, the dependency on r_{aH} was negligible at the mesic site (Tum) (Figs. 10i and 11i). Comparable patterns were found for the other sites listed in Table 2 (see Appendix, Fig. A1). The *LE* residual error for the semi-arid grassland site in northern Australia (Stp) also showed a strong relationship to r_{aM} and r_{aH} (see Fig. A1g,h,i). The dependencies on r_{aM} (r_{aH}) were not significantly reduced when models were constrained with in-situ *LST* (see Appendix, Fig. A5, Tables A1-A6).

H was slightly overestimated and *LE* was underestimated by all the three models at the water-limited sites (Cpr and Gin) when the difference between MODIS and in-situ *LST* was very high (Figs. 12 & 13 a,b,d, e,g,h). On the other hand, the underestimation (overestimation) of *H* (*LE*) at these sites was largely associated with a ΔLST near or below zero. For the mesic forest site (Tum), no substantial dependency on ΔLST was observed for SPARSE (Figs. 12c and 13c), but the findings for SEBS and STIC were contrasting (Figs. 12f,i and 13f,i), i.e., a high ΔLST coincided with underestimation (overestimation) of *H* by SEBS (STIC) and vice versa for *LE*. Similar findings from all models are confirmed for the other

sites presented in the Appendix (Fig. A2).

4.4. Regression analysis

In order to substantiate our findings from the previous sections, the relationship between the residual error of *LE* as final model output and a host of variables (see Section 2.3) was investigated by performing a PLSR analysis (Fig. 14). These variables and corresponding modelled *LE* signals were clustered for each set of arid, semi-arid and mesic sites (Table 2). If the Variable Importance in Projection (VIP) score exceeds a value of 0.8, the variable plays an important role in determining the *LE* residual error. The results indicated that for all models ΔLST, r_{aM} (or r_{aH}), *VPD* and F_c had a major impact on the *LE* residual error (Fig. 14). The influence of modelled Φ on the *LE* residuals was of minor importance for SPARSE, but was important for SEBS (mesic sites) and for STIC (all sites). A detailed evaluation of the accuracy of modelled Φ with SPARSE is presented in the Appendix (Fig. A3).

The most significant contribution of r_{aM} and r_{aH} to the residual *LE* error was found at the semi-arid sites, where it exceeded the influence of ΔLST for SPARSE and STIC (Fig. 14b,h). Interestingly, for SEBS, the role of kB^{-1} was found to be one of the major determinants in controlling the residual *LE* error in the water-limited ecosystems (VIP = 1.1 to 1.2) (Fig. 14d,e) in addition to the critical impact of r_{aM} in semi-arid ecosystems. The role of r_{aM} or r_{aH} on model uncertainty was greatly diminished at the mesic ecosystems as shown in Fig. 14 (c,f,i). Overall,
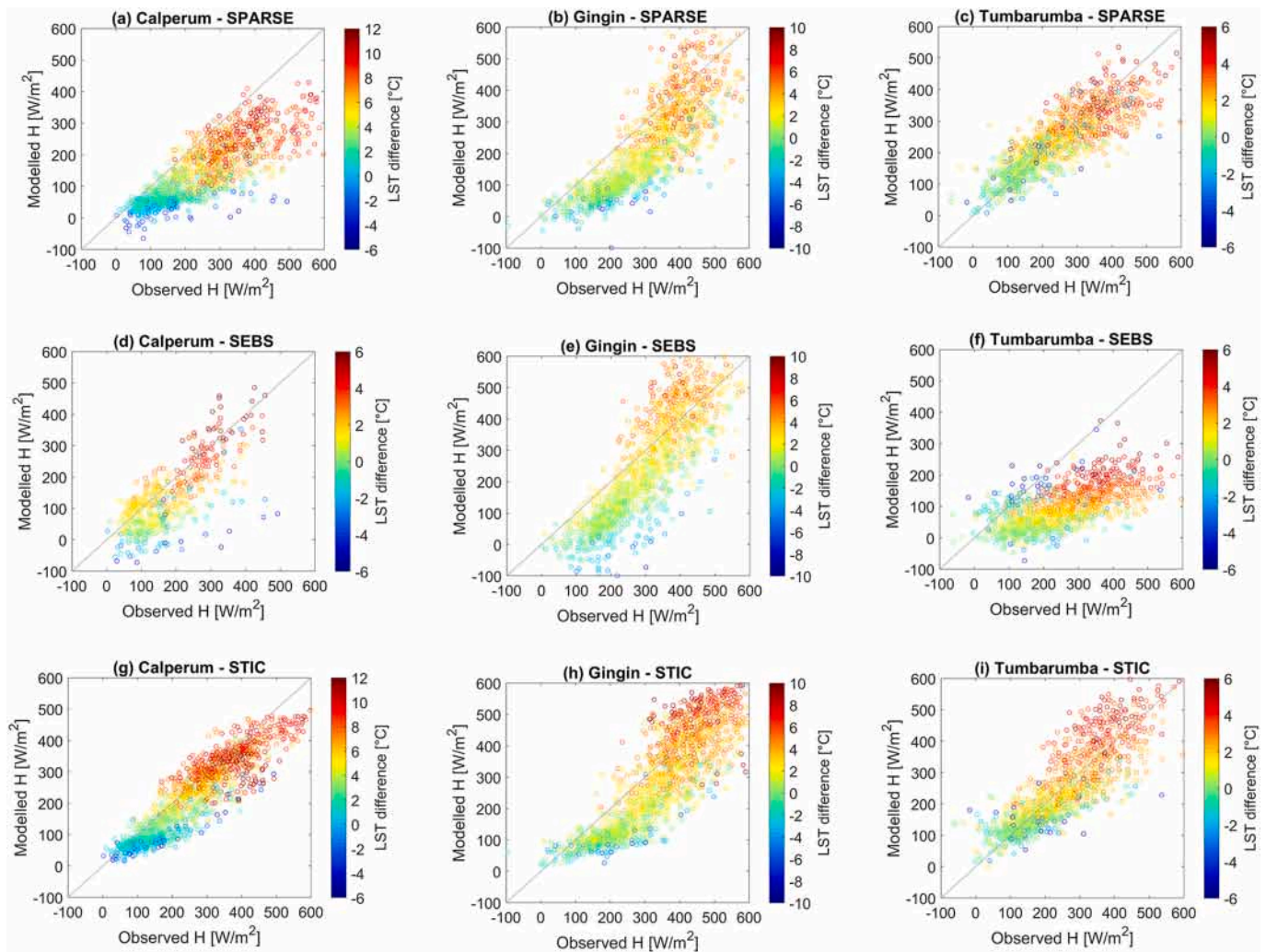
Fig. 12. Scatter plots of modelled *H* versus observed *H* color-coded with the difference between MODIS *LST* and in-situ *LST* (*ΔLST*) for SPARSE (a-c), SEBS (d-f) and STIC (g-i) for the representative arid (Cpr), semi-arid (Gin), and mesic (Tum) sites using MODIS *LST* as input to simulate *H* with the three models. For SEBS, omission of data with high *LST* values due to the dry limit required a different scaling of the *ΔLST* color bar for the site Cpr. Regression statistics are presented in Tables A1, A3 and A5.

the dependency of *LE* bias on r_{aM} in the water-limited ecosystems was slightly larger for the two-source model SPARSE as compared to the one-source models SEBS and STIC (r_{aH}), which is also reflected in the PLSR results for *H* (Fig. A4).

5. Discussion

In general, our results at the water-limited sites provided support for our hypothesis, revealing that the influence of r_{aM} (r_{aH}) on the instantaneous *LE* error is high in these ecosystems, where it can potentially be as large as the influence of uncertainties in *LST* (Fig. 14). Overestimation of *LE* by the models at the water-limited sites was found to coincide with high r_{aM} or r_{aH} (Fig. 7a,b, Fig. 9a,b) and is caused by an underestimation of *H*, which substantiates previous findings (Gokmen et al., 2012; Gokool et al., 2020; Morillas et al., 2013; Pardo et al., 2014; Seneviratne et al., 2010; van der Kwast et al., 2009). This reveals the tendency of underestimation (overestimation) of *H* (*LE*) under low wind speeds resulting in high r_{aM} or r_{aH} (predominantly between June and August, see Fig. 7). Under such conditions *ΔLST* was near zero or slightly negative (Fig. 8, Figs. 12 & 13), which implies that the substantial positive difference between MODIS *LST* and in-situ *LST* did not explain the positive model bias in *LE*. Instead, the positive *ΔLST* caused a slight overestimation of *H*, and, subsequently underestimation of *LE* at the

water-limited sites (Figs. 12 & 13), prevailing mainly during the dry season (Fig. 8 & Fig. 9a,b).

In contrast, mesic forest sites (Tum and Wom) showed either no underestimation (overestimation) of *H* (*LE*) (SPARSE and STIC) or the observed *H* underestimation (*LE* overestimation) indicated negligible dependency on r_{aM} or r_{aH} (SEBS), rejecting our hypothesis for these ecosystems. These ecosystems receive higher rainfall and have lower potential evaporative demand while retaining soil moisture more efficiently than sparse vegetation and grassland of arid and semi-arid ecosystems, which results in substantially higher SWC (Griebel et al., 2016; van Gorsel et al., 2016). Additionally, *LST* of forests is lower due to transpiration induced cooling, high surface roughness and strong turbulent mixing shown by low r_{aM} (Fig. 7) (Panwar et al., 2020).

5.1. Comparison of r_{aM} between SPARSE and SEBS

In general, r_{aM} (r_{aH}) cannot be directly measured in the field and is considered as an unobserved variable. In-situ r_a values are also obtained from friction velocity (or wind speed) and using MOST and Richardson number approaches (Banerjee et al., 2017; Liu et al., 2007), typically involving a constant kB^{-1} factor of two. Consequently, depending on the applied parameterization the "observed" r_{aM} or r_{aH} would be either comparable or different to the modelled r_{aM} or r_{aH}. Hence, in order to
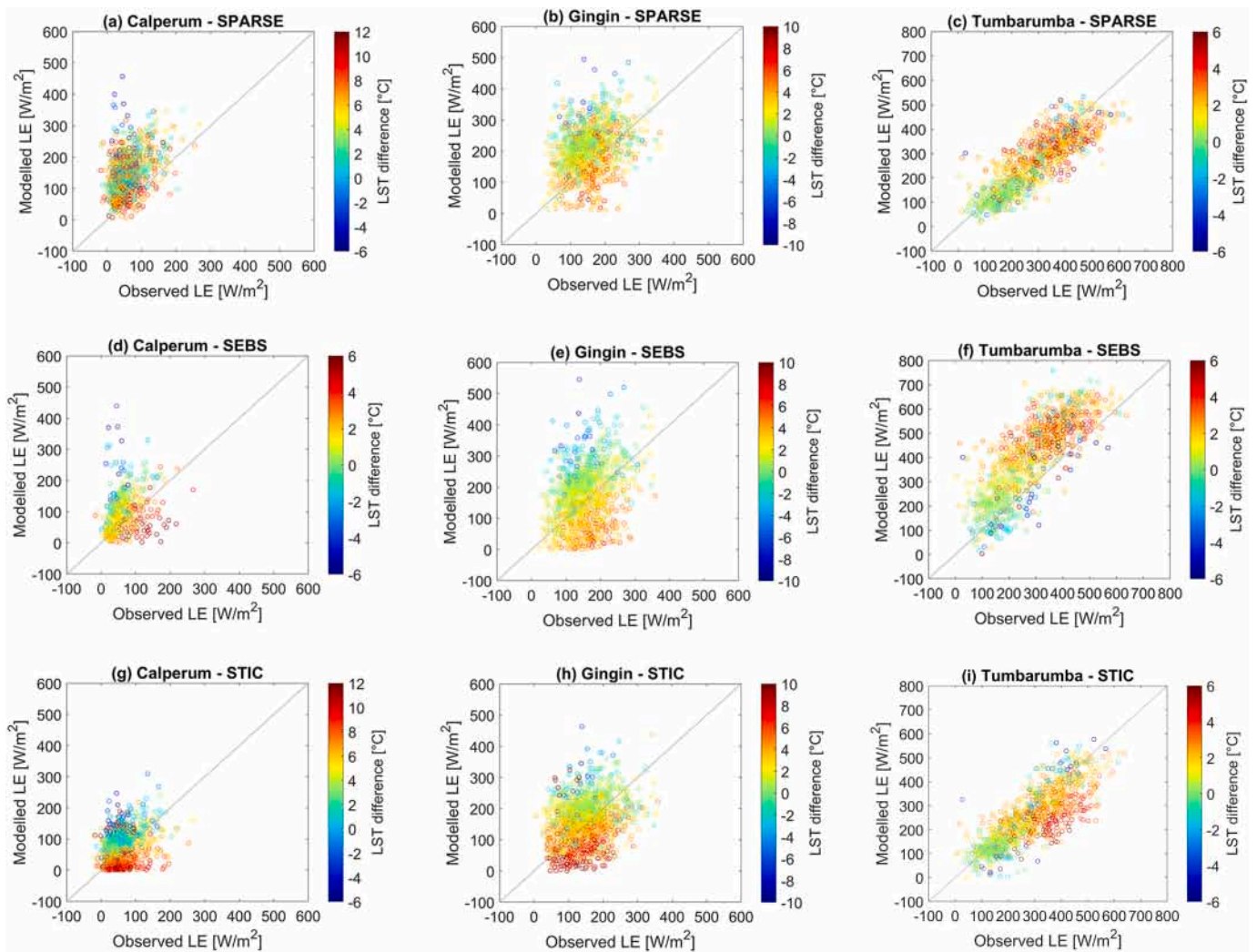
Fig. 13. Scatter plots of modelled *LE* versus observed *LE* color-coded with the difference between MODIS *LST* and in-situ *LST* (Δ*LST*) for SPARSE (a-c), SEBS (d-f) and STIC (g-i) for the representative arid (Cpr), semi-arid (Gin), and mesic (Tum) sites using MODIS *LST* as input to simulate *LE* with the three models. For SEBS, omission of data with high *LST* values due to the dry limit required a different scaling of the Δ*LST* color bar for the site Cpr. Regression statistics are presented in Tables A2, A4 and A6.

coherently identify the structural uncertainties of the models, their computed r_{aM} values were compared between each other. As the estimation of r_{aH} in STIC is different from the methods applied in SPARSE and SEBS (Table 1), the computation of r_{aM} from STIC is not straightforward. Therefore, we only compared the r_{aM} derived by SPARSE and SEBS (see Eqs. (3) and (4)). Fig. 15a,b shows that SEBS computes lower r_{aM} values than SPARSE for the water-limited sites (Cpr and Gin). Relatively good agreement between the two models was found at high wind speeds (falling nearly along the 1:1 line in Fig. 15a,b) when mechanical turbulence production dominates (near-neutral conditions). However, large discrepancies under unstable conditions (Fig. 15, datapoints falling below the 1:1 line) are attributed to the different approaches to account for atmospheric stability in the two models. In contrast, r_{aM} estimates from the two models for the mesic site (Tum) compared relatively well (except some outliers, Fig. 15c).

The stability correction term in r_{aM} is determined as a function of the Monin-Obukhov length scale (*L*) in SEBS (Brutsaert, 1992, 1999) and by the bulk Richardson number (R_{ib}) in SPARSE (Boulet et al., 2015) (Table 1). Both are computed through iteration either using *H* or aerodynamic temperature (T_0), which directly depend on LST that strongly determines the buoyancy production near the surface. Accurate quantification of buoyant versus mechanical turbulence production

influences the stability correction and the magnitude of r_a. Hence, in both models, r_{aM} and *LST* are intrinsically linked through the stability correction term and aerodynamic feedbacks on T_0, T_a and *H*. Although the discrepancies in r_{aM} between SPARSE and SEBS in Fig. 15 do not quantitatively explain the overestimation of *LE* by both models, it indicates substantial uncertainty associated with the empirical specification of r_{aM} that influences the model performance.

Additionally, seasonal effects on r_{aM} (Fig. 7) largely control the uncertainty in *LE*. During the winter wet season at Cpr and Gin, synoptic weather systems cause low wind speed conditions, thereby enhancing r_{aM} and the influence of the atmospheric stability correction terms. During winter, the subtropical ridge is at its northernmost position, away from southern Australia (Cai et al., 2011a), and subsidence on the western pole of the Southern Ocean reduces convection over Australia (Cai et al., 2011b), both of which thrust the southern Australian region into a calm wet season with low winds. Seasonal variations in SWC and humidity can also influence r_{aM} and stability in other arid or semi-arid locations (Cleverly et al., 2013). By example, at Cpr and Gin, SWC is always below 10% during wet and dry seasons, which limits evaporative cooling of the surface. In combination with low wind speeds, surface heating is intense and causes a strong surface layer stratification (Sun et al., 2020), which is not well represented by the stability correction
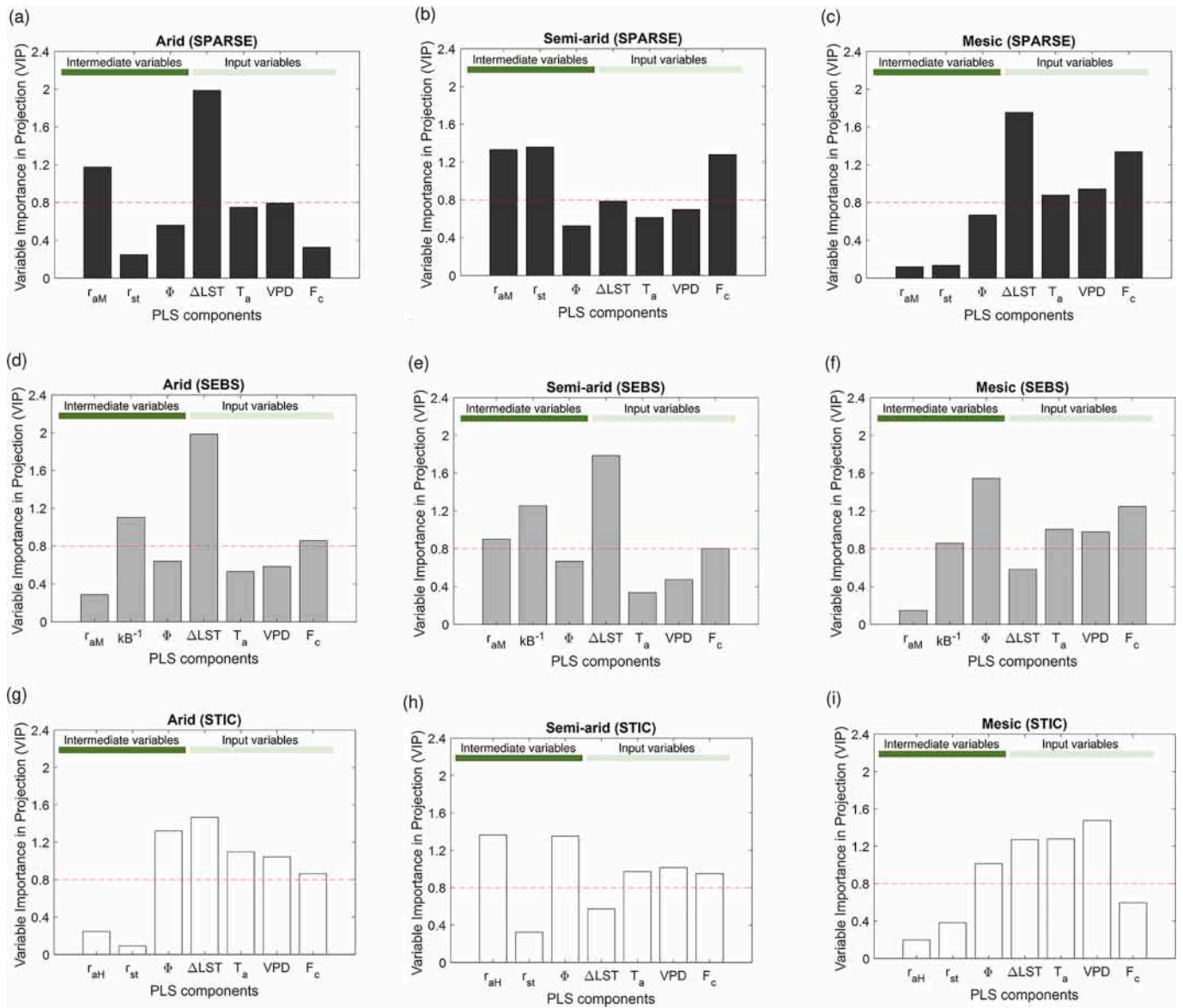
Fig. 14. Bar plots of the Variable Importance in Projection (*VIP*) scores for the residual error of *LE* involving r_{aM}, r_{aH}, KB^{-1} (SEBS), the stomata resistance (r_{st}) (SPARSE & STIC), modelled Φ with SPARSE, *LST* difference (ΔLST), air temperature (T_a), vapor pressure deficit (*VPD*) and F_c for SPARSE (a-c), SEBS (d-f) and STIC (g-i) for all the arid sites (clustered), semi-arid sites (clustered) and mesic sites (clustered) using MODIS *LST* as input to run the models. The dashed red line (VIP = 0.8) denotes the variable importance threshold. (For interpretation of the references to color in this figure legend, the reader is referred to the web version of this article.)
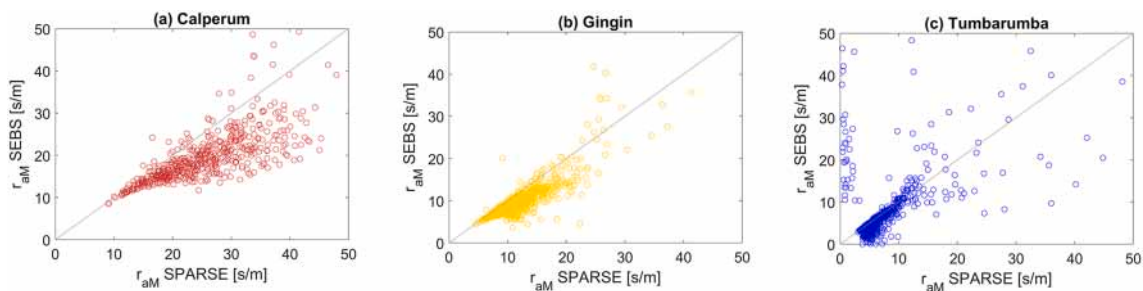
Fig. 15. Scatter plots of r_{aM} estimated by SEBS versus r_{aM} estimated by SPARSE for (a) Calperum, (b) Gingin and (c) Tumbarumba using MODIS *LST* as input to run the models.

terms. The identified differences in r_{aM} for both formulations are even higher in the shrubland and savanna ecosystems (ASM, Dry, DaS, not shown), at which, however, a negative bias in modelled *LE* was found for SEBS (Fig. 5).

5.2. Significance of model results

5.2.1. Empirical aerodynamic roughness parameters

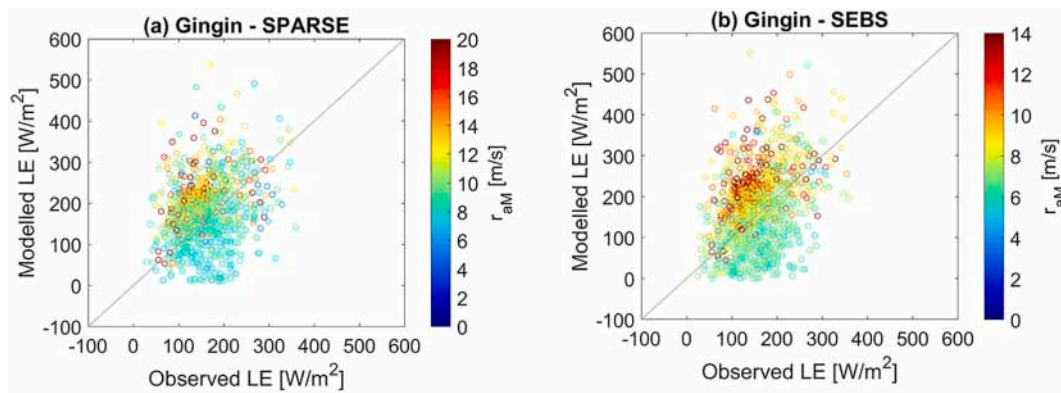The accurate representation of the aerodynamic parameters (z_{0m} and

Fig. 16. Scatter plots of modelled *LE* versus observed *LE* color-coded with r_{aM} for (a) SPARSE and (b) SEBS at the semi-arid site Gingin using MODIS *LST* and $d = 2.5$ m and $z_{0m} = 0.9$ m determined from vertical wind profiles as input to simulate *LE*. Regression statistics SPARSE: KGE = −0.07, RMSE = 103 W/m^2, MBE = −30 W/m^2, MAPE = 64%, R^2 = 0.09; SEBS: KGE = 0.08, RMSE = 91 W/m^2, MBE = 24 W/m^2, MAPE = 55%, R^2 = 0.11.

d) is a key ingredient for obtaining good model performance. Due to the seasonal variations in LAI and ecosystem structure, seasonal variation of these parameters should ideally be obtained (Zhou et al., 2012), which is, however, quite complex for sparse heterogeneous ecosystems. The application of empirical parameterizations to derive time-variant values of z_{0m} and *d* based on LAI (e.g., expressions from Colaizzi et al. (2004) and Pereira et al. (1999)) generally degraded the model performance of SPARSE (results not shown for brevity) and are not suitable for these specific Australian ecosystems. Likewise, time-variant aerodynamic parameters calculated by SEBS using NDVI-based canopy height, LAI and the canopy momentum transfer sub-model (Section 2.1.2) were lower than experimentally derived values and increased the *LE* model bias (overestimation) for the arid and semi-arid sites. For these reasons, the study was performed with constant *d* and z_{0m} directly derived from EC measurements for both SPARSE and SEBS (see Table 3). For comparison, the only available measured vertical profiles of horizontal wind speed at the semi-arid site Gin allowed for the direct retrieval of *d* and z_{0m}, which resulted in $d = 2.2$–2.9 m and $z_{0m} = 0.9$ m (personal communication, A. Kunadi). These values are different than the values presented in Table 3. Fig. 16a,b exemplarily shows simulations with the SPARSE and SEBS models with $d = 2.5$ m and $z_{0m} = 0.9$ m, from which the dependency of the *LE* residual error on r_{aM} is also evident.

While overall regression statistics did not improve significantly compared to the model runs with the original *d* and z_{0m} values (see Tables A2, A4), the MBE of SEBS increased slightly and the overestimation tendency of SPARSE was reversed (MBE changed from a positive to a negative value). This demonstrates the importance of accurate aerodynamic parameters for estimating *LE*, which are likely different from the standard empirical parameterizations in heterogeneous sparse ecosystems (e.g. $d < 0.6h_c$). They also contribute to the accuracy of the stability correction functions and may vary with LAI and wind direction, making their quantification and application in SEB models extremely challenging.

5.2.2. Impact of the underlying soil and understory vegetation

For the two-source model SPARSE, the formulations of soil-air and canopy-air aerodynamic resistances may play an additional role in controlling the uncertainty of *LE*. Previous studies reported that novel soil parameterizations and explicitly incorporating the understory aerodynamic exchange significantly improves two-source model estimates of *H* and *LE* in the sparsely vegetated ecosystems (e.g. Li et al., 2019). Haghighi and Or (2015) developed a physically based model describing a soil resistance formulation for turbulent heat transport. Results show the enhancement of evaporative fluxes from bluff-rough surfaces relative to smooth flat surfaces under similar conditions. This new scheme has been successfully applied to semi-arid ecosystems where a meaningful reduction in the SEB flux retrieval error was found

(Haghighi and Kirchner, 2017). Considering these findings, it is likely that the underestimation (overestimation) of *H* (*LE*) by SPARSE might be partly attributed to the representation of the soil-air or understory-air aerodynamic exchange. However, our results indicate that overestimation of *LE* is primarily related to exchanges above the aerodynamic level (r_{aM}) and the associated buoyancy production intensity. This is supported by the fact that although some savanna sites (e.g. DaS) have sparse tree cover and substantial fluctuation in LAI between the dry and wet seasons (caused by dormant grass and bare soil patches) (Table 3), *LE* is not overestimated for these sites. On the other hand, *H* (*LE*) is also underestimated (overestimated) substantially for the semi-arid grassland site Stp, where an understory is absent. This suggests a minor influence of the soil aerodynamic exchange parameterization of SPARSE in our study. Since the one-source models SEBS and STIC also overestimated *LE*, we conclude that a significant fraction of uncertainty in all models can be attributed to r_{aM} and r_{aH}.

5.2.3. Influence of radiometric kB^{-1} in SEBS

The principal differences between observed and modelled *LE* of SEBS in the arid and semi-arid ecosystems are also due to kB^{-1} (Fig. 14d,e), which is a correction applied to circumvent the large differences between *LST* and T_0 in such ecosystems. Here, the role of z_{0h} becomes critical, which is estimated empirically through the kB^{-1} factor (Paul et al., 2014). Despite the first order dependence of kB^{-1} on *LST*, radiation, and meteorological variables, no physical model of kB^{-1} is available (Paul et al., 2014; Bhattarai et al., 2018) and uncertainties in kB^{-1} estimation are propagated into z_{0h}. Overestimation (or underestimation) of z_{0h} would lead to an overestimation (underestimation) of r_{aH} in SEBS, which is reflected in the *LE* residual error. Bhattarai et al. (2018) obtained a logarithmic pattern and significant correlation between the *LE* residual error and kB^{-1}.

The underestimation (overestimation) of *H* (*LE*) by SEBS for the mesic forest sites Wom and Tum might be associated with an overestimation of kB^{-1} and more specifically the canopy fraction of the kB^{-1} factor (Chen et al., 2019a). Chen et al. (2019a, 2019b) suggested that the overestimation of kB^{-1} for forest canopies in SEBS can be overcome by an improved column canopy-air turbulent transfer model that accounts for the momentum and heat transfer efficiency in different canopy vertical layers. While modification of the SEBS model is out of the scope of this study, this finding warrants future investigation using the SEBS model with an improved kB^{-1} parameterization for forest canopies.

5.2.4. LST uncertainties

Water-limited ecosystems are more prone to mismatch of tower flux footprint and hemispherical radiometric footprint due to their heterogeneous vegetation composition as compared to the mesic ecosystems (Marcolla and Cescatti, 2018; Morillas et al., 2013; Vivoni et al., 2010).

We postulate that neither in-situ *LST* nor MODIS *LST* is representative of the EC footprint as in-situ *LST* is typically measured by longwave radiation sensors directly mounted at the tower at the same or at a lower level than the EC measurements. Consequently, the origin of the radiation signal is not representative of the total EC flux footprint (Marcolla and Cescatti, 2018). Although the selected Australian ecosystems are reasonably homogeneous within a distance of 1 km to the tower, MODIS *LST* and in-situ *LST* were often different, especially for arid and semi-arid ecosystems with sparse vegetation during the dry season (Fig. 8). Flux towers are generally shorter in these ecosystems (lower vegetation height) as compared to forests, and, thus shorter towers lead to smaller footprints of the net radiometer. Moreover, different MODIS viewing configurations at sites with large heterogeneity as well as atmospheric corrections may contribute to the discrepancies (Chen et al., 2017).

An additional reason for the discrepancy between MODIS and in-situ *LST* could be the surface emissivity values calculated by Eq. (5). In general, the derived values compared relatively well to MODIS broad-band emissivities (ranging from 0.972 for arid heterogeneous sites to 0.983 for forests), which, however, do not represent seasonal variations. The dependency of soil emissivity on soil moisture and soil geological properties was not taken into account, and assuming that soil emissivity used in Eq. (5) could potentially be lower than 0.96 in shrubland and woodland ecosystems with high aridity (Jin and Liang, 2006), higher in-situ *LST* values would be derived which reduces the discrepancy with MODIS *LST*.

Given the absence of major improvements in the model results with in-situ *LST*, it appears that uncertainties in the empirical characterization of r_{aM} and r_{aH} tend to contribute substantially to the uncertainty in both SPARSE and SEBS. On the contrary, the theoretical assumptions in STIC, particularly the linearity of saturation vapor pressure versus temperatures to compute the psychrometric slopes and symmetrical assumptions in the advection-aridity hypothesis to obtain the closure equation of evaporative fraction tend to be the main source of uncertainty propagation in *LE* through r_{aH} (Mallick et al., 2015, 2016).

5.2.5. Accuracy of flux measurements

Another important aspect of our analysis is that the typical measurement error for *LE* of about 30 W/m^2 (Foken, 2017; Novick and Katul, 2020) is large compared to its absolute value in water-limited ecosystems. This introduces some uncertainty in our findings, as the accuracy of the EC method to derive *LE* is limited under these dry conditions when *H* is the dominating flux. Differences between modelled and observed *LE* may be partly attributed to the BREB-closure correction of *LE* observations. Mean values of the SEB closure at MODIS Terra and Aqua overpass times ranged from 74% to 93% (Table 3), which is comparable to values typically reported in the literature (Mauder et al., 2020). Mallick et al. (2018a) demonstrated that in the arid and semi-arid ecosystems, major corrections are generally observed in *H*, whereas correction in *LE* is negligible. Their study revealed significant correlations between the *LE* error statistics and BREB-closure corrections. In most of the arid and semi-arid sites, high MAPE and systematic RMSE in *LE* (>50%) was associated with low closure correction in *LE* (Mallick et al., 2018a).

5.2.6. Effect of modelled net available energy

Modelled Φ by SPARSE was slightly underestimated for most of the sites with MBE ranging from −40 W/m^2 (Tum) to −22 W/m^2 (Cal and DaS) (Fig. A3). Stp was the only site for which a small overestimation of Φ was found (MBE = 21 W/m^2). In general, underestimation of Φ causes underestimation of *LE* (Figs. 4-6), which diminishes the effects of the underestimation of *H* due to high r_{aM} and r_{aH}. For SPARSE, modelled Φ did not significantly contribute to the *LE* residual error, while for SEBS Φ strongly influenced the *LE* residual error of mesic ecosystems (Fig. 14f). Due to the nature of the evaporative fraction equation in SEBS (see Section 4), the difference between Φ and modelled *LE* was marginal near the wet limit, which resulted in a substantial underestimation of *H* at the forest sites Wom and Tum (Fig. 5a, Fig. 10f). Any condition that

produces $H \approx H_{wet}$ would tend to simulate substantially high relative evaporation ($\Lambda_r \approx 1$) and *LE* will be consequently overestimated. Mallick et al. (2018b) reported a systematic linear relationship between the residual daily ET error with daily Λ_r.

Results obtained with STIC indicated strong influence of Φ on the *LE* residual error for all ecosystem types, which was comparable to the impact of r_{aH} for semi-arid ecosystems. The more predominant role of Φ in STIC can be explained by its use for the calculation of r_{aH} (see Table 1).

6. Conclusion

The representation of the aerodynamic resistance for momentum and heat (r_{aM} and r_{aH}) determines the quality and consistency of thermal remote sensing-based surface energy balance (SEB) models for estimating *ET* (*LE*) in arid and semi-arid ecosystems and during drought. Moreover, r_{aM} (r_{aH}) is tightly coupled with *LST* through both atmospheric stability and aerodynamic feedback, which implies that their interaction influences the accuracy of *ET* estimates. However, until now the pivotal role of r_{aM} and r_{aH} has been largely underexplored as most previous studies have focused on the role of the kB^{-1} factor. For the first time, this work provides insights into the uncertainties of three structurally different SEB models and their relationship to r_{aM} (r_{aH}) and land surface temperature (*LST*) across a wide range of biomes and contrasting aridities. Evaluating the SEB models for the period 2011–2019 over nine Australian OzFlux sites using *LST* from both MODIS and in-situ observations as forcing led us to the following conclusions:

(a) The seasonality of r_{aM} (r_{aH}) calculated with three SEB models mirrored the seasonal variation of the difference between MODIS *LST* and in-situ *LST*, which implies that in general, high r_{aM} (r_{aH}) values coincide with a low *LST* difference and vice versa.

(b) Overall model performance to estimate instantaneous *H* and *LE* was relatively poor for arid and semi-arid sites with both sparse and dense vegetation, but it substantially improved for the mesic forest sites. While *LE* overestimation was attributed to inadequate accounting of soil and vegetation characteristics under water stress in previous studies (e.g., Gokool et al., 2020; Li et al., 2019; Kustas et al., 2016; Pardo et al., 2014), our results suggest that r_{aM} (r_{aH}) is overestimated at arid and semi-arid sites, particularly under unstable conditions when thermally generated turbulent mixing dominates. For two water-limited sites in southern Australia, this is most predominant during the winter wet season when low wind speeds prevail. This caused an underestimation of *H*, and consequently overestimation of instantaneous *LE*. Low r_{aM} resulted in marginal underestimation of *LE*, which was associated with a positive *LST* difference during the dry season.

(c) The accurate specification of aerodynamic parameters to determine r_{aM} is very challenging for sparse and heterogeneous ecosystems and contributes to the uncertainty in *LE* estimates. Although STIC retrieves r_{aH} independently from any empirical parameterization, it also showed a comparable dependency of the model bias on r_{aH} as SEBS and SPARSE for water-limited ecosystems. PLSR analysis revealed that at the semi-arid sites the effect of r_{aM} (r_{aH}) on the *LE* residual error can be of the same magnitude as the influence of uncertainties in *LST*. This dependency is not found for mesic forest ecosystems, where a high roughness length and low *LST* results in dominance of mechanically generated turbulence.

(d) As the magnitude of *H* becomes large compared to *LE* during drought, a small relative error in *H* due to uncertainties in r_{aM} or r_{aH} will propagate into a large relative error in *LE*. Our findings for dry Australian ecosystems question the accuracy with which instantaneous *LE* is modelled with current r_{aM} (r_{aH}) specification approaches in the contemporary SEB models, which is likely related to inadequate stability correction functions and uncertain

approaches to determine aerodynamic roughness parameters. Hence, novel approaches to estimate r_{aM} (r_{aH}) are required to enhance the performance of the SEB models in water-scarce environments.

Author contributions

IT and KM conceptualized the idea; IT organized the study and conducted SPARSE model simulations in consultation with GB; STIC and SEBS model simulations were made by KM and NB; IT made the data analysis in consultation with KM; IT wrote the first version of the manuscript; all authors contributed to discussions and corrections; IT and KM jointly finalized the manuscript.

Declaration of Competing Interest

None.

Appendix A

Table A1

Summary statistics of the SPARSE model performance (parallel version, retrieval mode) for the instantaneous *H* retrievals at satellite overpass times (MODIS Aqua and Terra) for nine sites of contrasting aridity in Australia. KGE: Kling-Gupta efficiency, RMSE: Root Mean Square Error, MBE: Mean Bias Error, MAPE: Mean absolute percentage error, R^2: Squared Pearson Correlation Coefficient, N: Number of data points retained for evaluation (LST$_{mod}$: MODIS *LST* was used as input, LST$_{insitu}$: in-situ *LST* was used as input).

Site	KGE	RMSE (W/m^2)	MBE (W/m^2)	MAPE (%)	R^2	N
input	LST$_{mod}$ (LST$_{in-situ}$)	LST$_{mod}$ (LST$_{in-situ}$)	LST$_{mod}$ (LST$_{in-situ}$)	LST$_{mod}$ (LST$_{in-situ}$)	LST$_{mod}$ (LST$_{in-situ}$)	LST$_{mod}$ (LST$_{in-situ}$)
Alice Springs	0.6 (0.53)	89 (163)	−49 (−153)	18 (42)	0.56 (0.73)	1094 (2201)
Calperum	0.6 (0.2)	117 (180)	−90 (−158)	39 (60)	0.65 (0.59)	1477 (1719)
Great Western Woodlands	0.62 (0.31)	122 (195)	−96 (−176)	35 (56)	0.68 (0.54)	1329 (1572)
Gingin	0.53 (0.6)	114 (143)	−57 (−125)	38 (45)	0.74 (0.74)	1707 (2057)
Sturt Plains	0.28 (0.23)	133 (147)	−109 (−133)	44 (52)	0.19 (0.3)	1923 (1982)
Dry River	0.54 (0.51)	98 (95)	−19 (3)	37 (41)	0.3 (0.28)	1487 (1494)
Wombat	0.75 (0.76)	83 (69)	13 (−33)	31 (25)	0.7 (0.77)	1307 (1374)
Daly Uncleared	0.5 (0.56)	97 (81)	43 (20)	43 (29)	0.28 (0.33)	1023 (1526)
Tumbarumba	0.75 (0.7)	68 (70)	−9 (−18)	33 (30)	0.68 (0.67)	1519 (1533)

Table A2

Summary statistics of the SPARSE model performance (parallel version, retrieval mode) for the instantaneous *LE* retrievals at satellite overpass times (MODIS Aqua and Terra) for nine sites of contrasting aridity in Australia. Detailed description see Table A1.

Site	KGE	RMSE (W/m^2)	MBE (W/m^2)	MAPE (%)	R^2	N
input	LST$_{mod}$ (LST$_{in-situ}$)	LST$_{mod}$ (LST$_{in-situ}$)	LST$_{mod}$ (LST$_{in-situ}$)	LST$_{mod}$ (LST$_{in-situ}$)	LST$_{mod}$ (LST$_{in-situ}$)	LST$_{mod}$ (LST$_{in-situ}$)
Alice Springs	0.17 (−1.92)	79 (146)	19 (135)	514 (1822)	0.28 (0.53)	1094 (2201)
Calperum	−0.7 (−2.1)	95 (171)	68 (155)	280 (564)	0.16 (0.14)	1477 (1719)
Great Western Woodlands	−0.62 (−1.6)	98 (180)	60 (162)	204 (435)	0.08 (0.07)	1329 (1572)
Gingin	−0.02 (0.08)	97 (120)	22 (97)	67 (93)	0.14 (0.17)	1707 (2057)
Sturt Plains	−0.39 (−0.72)	150 (172)	129 (160)	675 (837)	0.61 (0.69)	1923 (1982)
Dry River	0.74 (0.61)	87 (92)	−15 (−37)	70 (66)	0.56 (0.51)	1487 (1494)
Wombat	0.61 (0.76)	97 (69)	−50 (−0.1)	31 (25)	0.5 (0.63)	1307 (1374)
Daly Uncleared	0.55 (0.71)	105 (77)	−64 (5)	69 (76)	0.53 (0.52)	1023 (1526)
Tumbarumba	0.79 (0.83)	72 (68)	−29 (−14)	30 (30)	0.72 (0.73)	1519 (1533)

Table A3

Summary statistics of the SEBS model performance for the instantaneous *H* retrievals at satellite overpass times (MODIS Aqua and Terra) for nine sites of contrasting aridity in Australia. Detailed description see Table A1.

Site	KGE	RMSE (W/m^2)	MBE (W/m^2)	MAPE (%)	R^2	N
input	LST$_{mod}$ (LST$_{in-situ}$)	LST$_{mod}$ (LST$_{in-situ}$)	LST$_{mod}$ (LST$_{in-situ}$)	LST$_{mod}$ (LST$_{in-situ}$)	LST$_{mod}$ (LST$_{in-situ}$)	LST$_{mod}$ (LST$_{in-situ}$)
Alice Springs	0.19 (0.34)	156 (74)	−12 (−34)	48 (20)	0.1 (0.66)	146 (655)
Calperum	0.61 (0.6)	87 (111)	−46 (−73)	50 (40)	0.55 (0.57)	578 (1271)
Great Western Woodlands	0.55 (0.79)	72 (77)	−20 (−36)	30 (20)	0.59 (0.73)	429 (1121)
Gingin	0.46 (0.64)	110 (125)	−56 (−107)	44 (45)	0.72 (0.8)	1306 (1724)

(continued on next page)

Table A3 (*continued*)

Site	KGE	RMSE (W/m^2)	MBE (W/m^2)	MAPE (%)	R^2	N
input	LST$_{mod}$ (LST$_{in\text{-}situ}$)	LST$_{mod}$ (LST$_{in\text{-}situ}$)	LST$_{mod}$ (LST$_{in\text{-}situ}$)	LST$_{mod}$ (LST$_{in\text{-}situ}$)	LST$_{mod}$ (LST$_{in\text{-}situ}$)	LST$_{mod}$ (LST$_{in\text{-}situ}$)
Sturt Plains	0.56 (0.64)	83 (70)	−27 (−29)	30 (25)	0.38 (0.5)	1027 (1391)
Dry River	0.48 (0.63)	101 (82)	−11 (48)	45 (49)	0.24 (0.53)	923 (987)
Wombat	0.28 (−0.04)	190 (241)	−168 (−222)	66 (83)	0.52 (0.67)	1110 (1112)
Daly Uncleared	0.45 (0.67)	96 (69)	22 (−17)	45 (26)	0.25 (0.47)	759 (1327)
Tumbarumba	0.13 (−0.16)	178 (220)	−152 (−193)	72 (81)	0.4 (0.23)	1375 (1378)

Table A4
Summary statistics of the SEBS model performance for the instantaneous *LE* retrievals at satellite overpass times (MODIS Aqua and Terra) for nine sites of contrasting aridity in Australia. Detailed description see Table A1.

| Site	KGE	RMSE (W/m^2)	MBE (W/m^2)	MAPE (%)	R^2	N
input	LST$_{mod}$ (LST$_{in\text{-}situ}$)	LST$_{mod}$ (LST$_{in\text{-}situ}$)	LST$_{mod}$ (LST$_{in\text{-}situ}$)	LST$_{mod}$ (LST$_{in\text{-}situ}$)	LST$_{mod}$ (LST$_{in\text{-}situ}$)	LST$_{mod}$ (LST$_{in\text{-}situ}$)
Alice Springs	0.27 (0.75)	162 (65)	−19 (13)	278 (106)	0.09 (0.65)	146 (655)
Calperum	−0.14 (−0.71)	74 (98)	37 (72)	128 (270)	0.07 (0.26)	578 (1271)
Great Western Woodlands	−0.04 (0.13)	84 (75)	15 (26)	94 (108)	0.08 (0.09)	429 (1121)
Gingin	0.06 (0.24)	91 (101)	17 (79)	54 (74)	0.09 (0.31)	1306 (1724)
Sturt Plains	0.62 (0.48)	92 (82)	50 (58)	154 (243)	0.72 (0.81)	1027 (1391)
Dry River	0.68 (0.57)	97 (103)	−23 (−83)	56 (47)	0.57 (0.74)	923 (987)
Wombat	0.33 (0.08)	156 (214)	130 (189)	65 (90)	0.55 (0.53)	1110 (1112)
Daly Uncleared	0.54 (0.75)	102 (66)	−43 (2)	48 (54)	0.58 (0.71)	759 (1327)
Tumbarumba	0.48 (0.25)	145 (191)	113 (160)	67 (81)	0.66 (0.67)	1375 (1378)

Table A5
Summary statistics of the STIC model performance for the instantaneous *H* retrievals at satellite overpass times (MODIS Aqua and Terra) for nine sites of contrasting aridity in Australia. Detailed description see Table A1.

Site	KGE	RMSE (W/m^2)	MBE (W/m^2)	MAPE (%)	R^2	N
input	LST$_{mod}$ (LST$_{in\text{-}situ}$)	LST$_{mod}$ (LST$_{in\text{-}situ}$)	LST$_{mod}$ (LST$_{in\text{-}situ}$)	LST$_{mod}$ (LST$_{in\text{-}situ}$)	LST$_{mod}$ (LST$_{in\text{-}situ}$)	LST$_{mod}$ (LST$_{in\text{-}situ}$)
Alice Springs	0.71 (0.58)	73 (105)	−39 (−79)	17 (25)	0.7 (0.71)	2228 (2228)
Calperum	0.83 (0.7)	63 (85)	−36 (−65)	22 (29)	0.83 (0.81)	1719 (1719)
Great Western Woodlands	0.81 (0.79)	75 (81)	−35 (−54)	18 (21)	0.71 (0.76)	1586 (1586)
Gingin	0.72 (0.65)	93 (124)	−50 (−100)	33 (41)	0.75 (0.71)	2068 (2068)
Sturt Plains	0.46 (0.45)	84 (85)	14 (7)	32 (33)	0.35 (0.29)	1984 (1984)
Dry River	0.58 (0.5)	98 (106)	−7 (15)	45 (52)	0.33 (0.26)	1814 (1814)
Wombat	0.72 (0.49)	91 (117)	−50 (−85)	38 (43)	0.65 (0.62)	1374 (1374)
Daly Uncleared	0.52 (0.52)	93 (93)	23 (−21)	38 (38)	0.31 (0.31)	1662 (1662)
Tumbarumba	0.83 (0.59)	69 (77)	−4 (−41)	37 (38)	0.7 (0.73)	1536 (1536)

Table A6
Summary statistics of the STIC model performance for the instantaneous *LE* retrievals at satellite overpass times (MODIS Aqua and Terra) for nine sites of contrasting aridity in Australia. Detailed description see Table A1.

Site	KGE	RMSE (W/m^2)	MBE (W/m^2)	MAPE (%)	R^2	N
input	LST$_{mod}$ (LST$_{in\text{-}situ}$)	LST$_{mod}$ (LST$_{in\text{-}situ}$)	LST$_{mod}$ (LST$_{in\text{-}situ}$)	LST$_{mod}$ (LST$_{in\text{-}situ}$)	LST$_{mod}$ (LST$_{in\text{-}situ}$)	LST$_{mod}$ (LST$_{in\text{-}situ}$)
Alice Springs	0.51 (−0.21)	63 (89)	8 (61)	407 (886)	0.31 (0.38)	2228 (2228)
Calperum	0.22 (−0.31)	50 (76)	14 (63)	144 (266)	0.11 (0.23)	1719 (1719)
Great Western Woodlands	0.21 (0.04)	65 (70)	−0.8 (40)	110 (151)	0.04 (0.1)	1586 (1586)
Gingin	0.25 (0.12)	76 (100)	15 (72)	54 (82)	0.08 (0.07)	2068 (2068)
Sturt Plains	0.64 (0.56)	80 (85)	6 (20)	300 (404)	0.5 (0.46)	1984 (1984)
Dry River	0.54 (0.26)	101 (119)	−27 (−49)	60 (59)	0.38 (0.2)	1814 (1814)
Wombat	0.7 (0.57)	80 (102)	14 (53)	29 (39)	0.53 (0.53)	1374 (1374)
Daly Uncleared	0.54 (0.53)	98 (92)	−44 (6)	55 (78)	0.38 (0.31)	1662 (1662)
Tumbarumba	0.76 (0.84)	80 (66)	−35 (8)	28 (27)	0.67 (0.76)	1536 (1536)
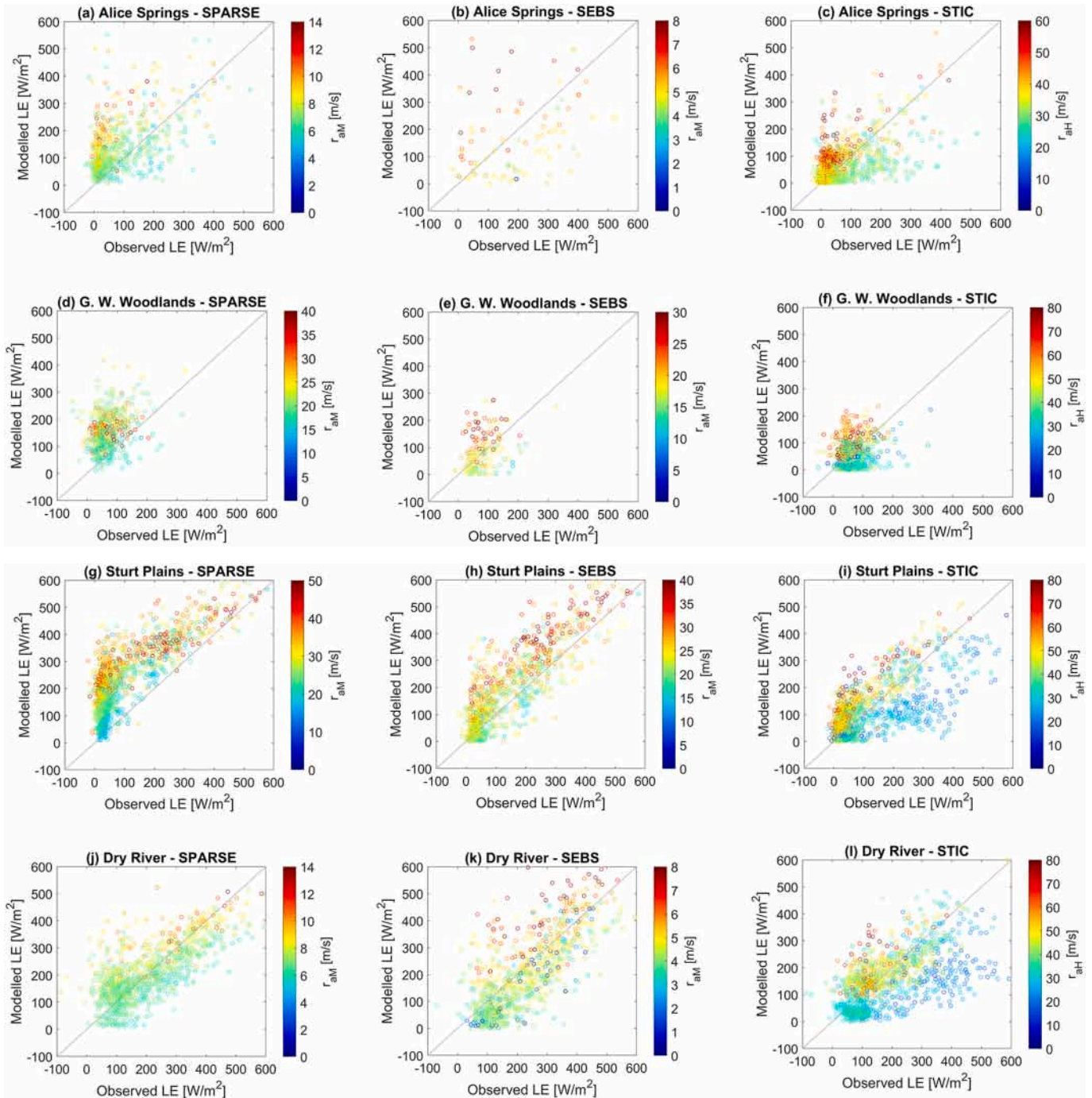
Fig. A1. Scatter plots of modelled *LE* versus observed *LE* color-coded with r_{aM} for SPARSE (left panel), SEBS (middle panel) and r_{aH} for STIC (right panel) for Alice Springs (a-c), Great Western Woodlands (d-f), Sturt Plains (g-i), Dry River (j-l), Wombat (m-o) and Daly Uncleared (p-r) using MODIS *LST* as input to run the models.
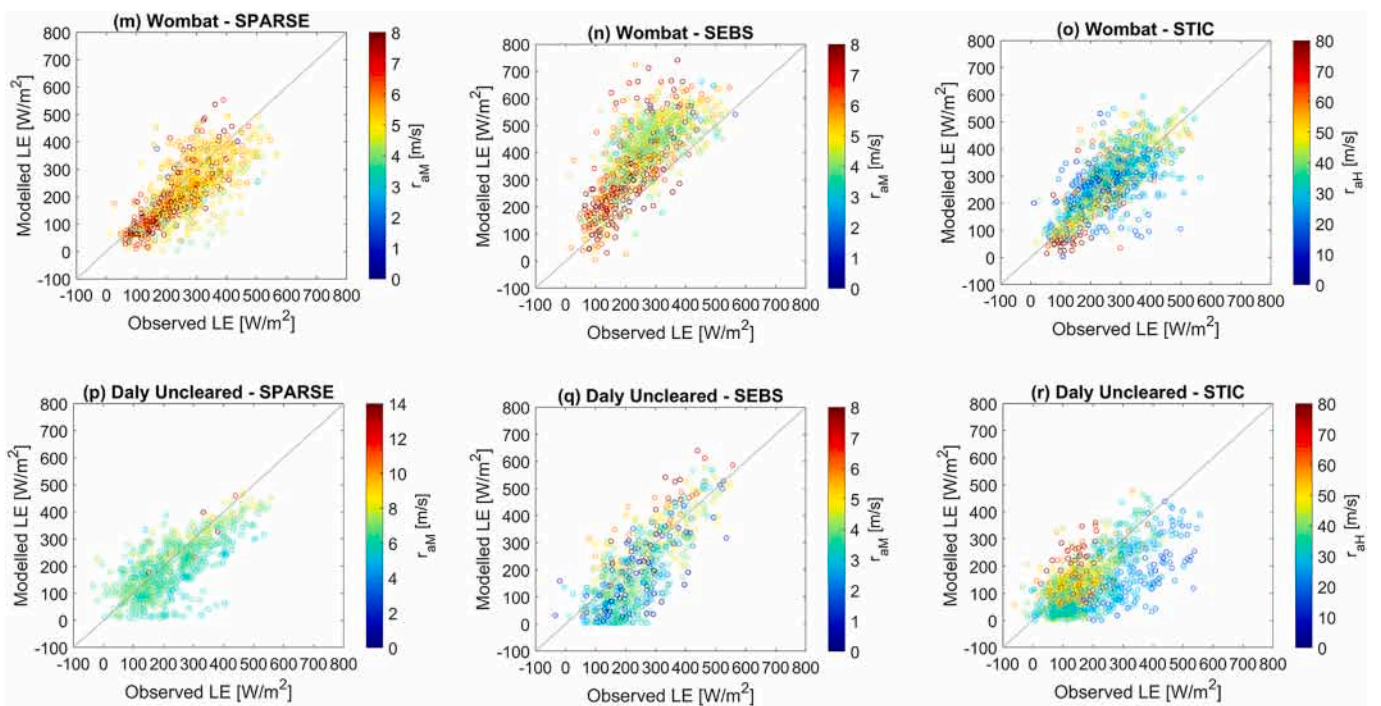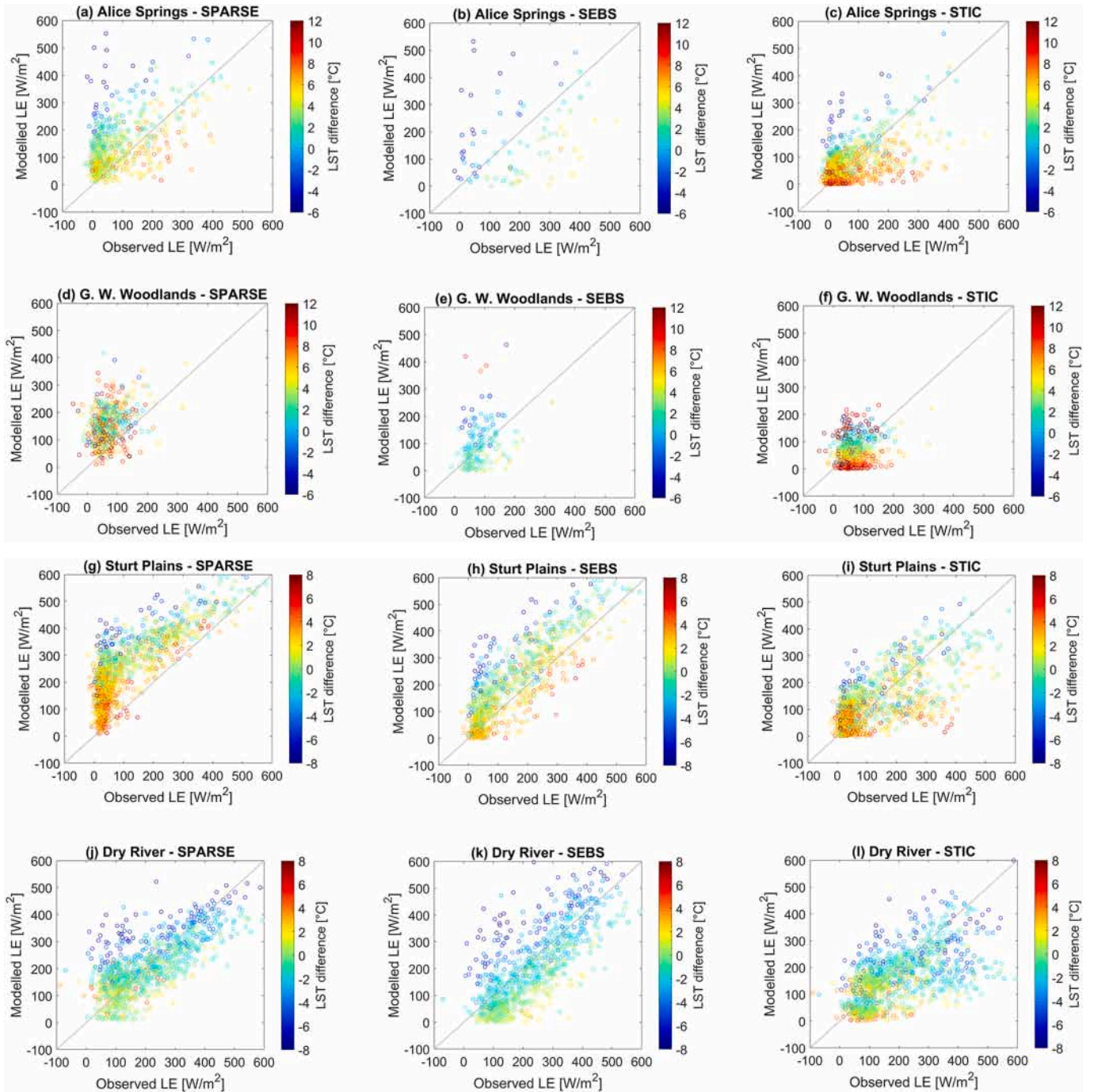
Fig. A1. (*continued*).

Fig. A2. Scatter plots of modelled *LE* versus observed *LE* color-coded with the difference between MODIS *LST* and in-situ *LST* for SPARSE (left panel), SEBS (middle panel) and STIC (right panel) for Alice Springs (a-c), Great Western Woodlands (d-f), Sturt Plains (g-i), Dry River (j-l), Wombat (m-o) and Daly Uncleared (p-r) using MODIS *LST* as input to run the models.
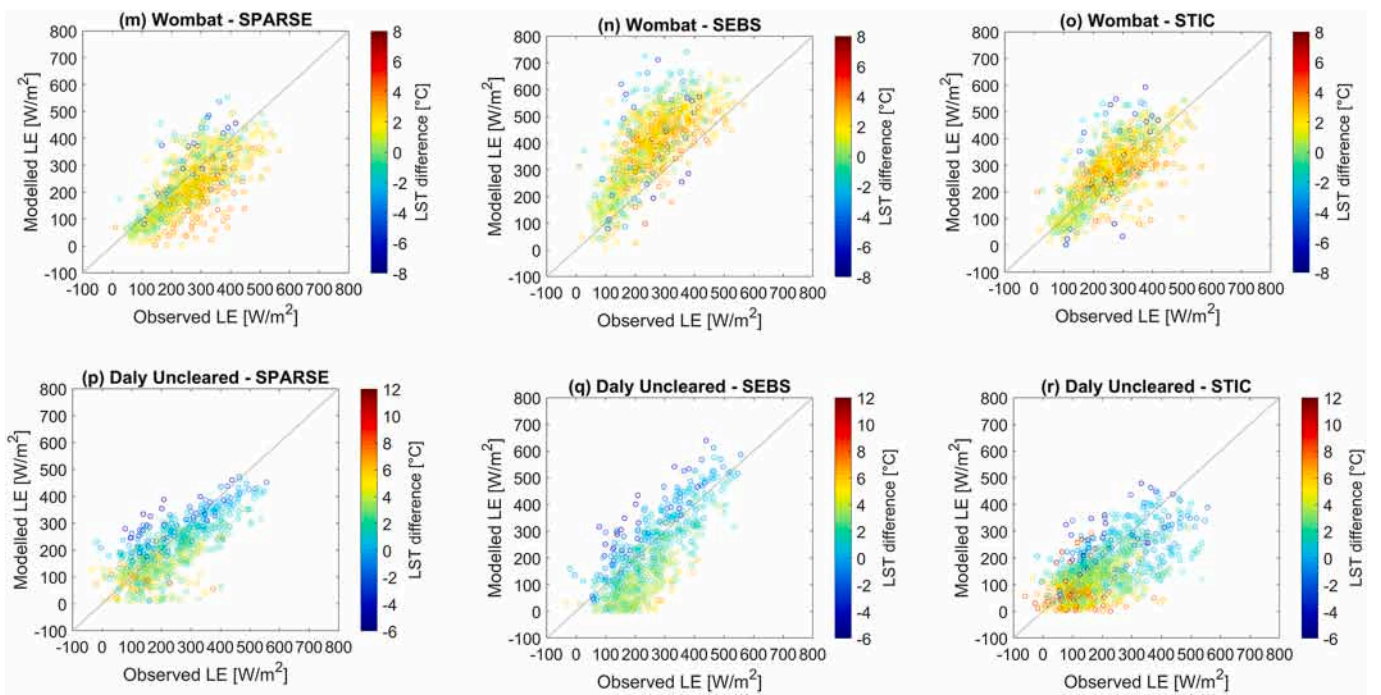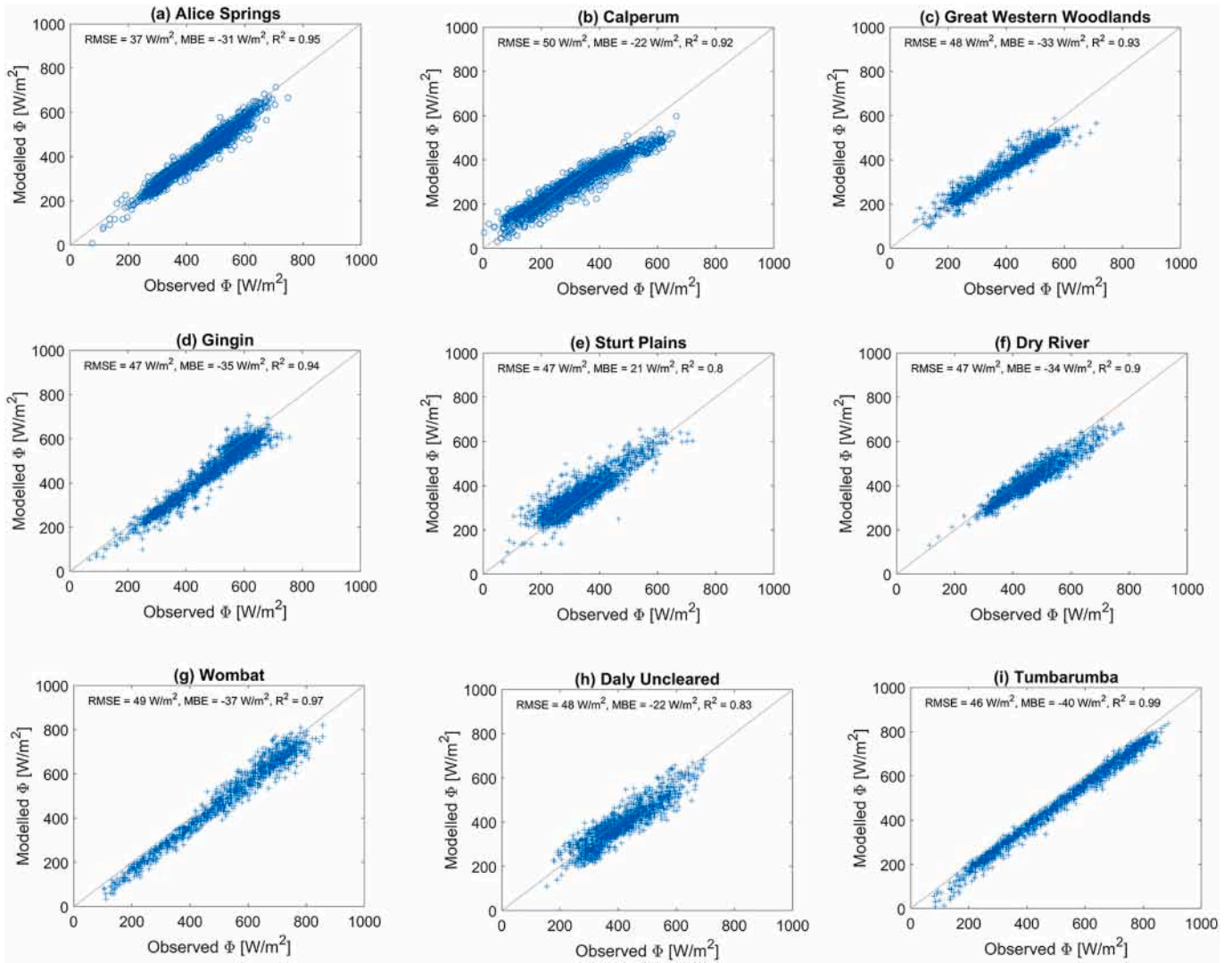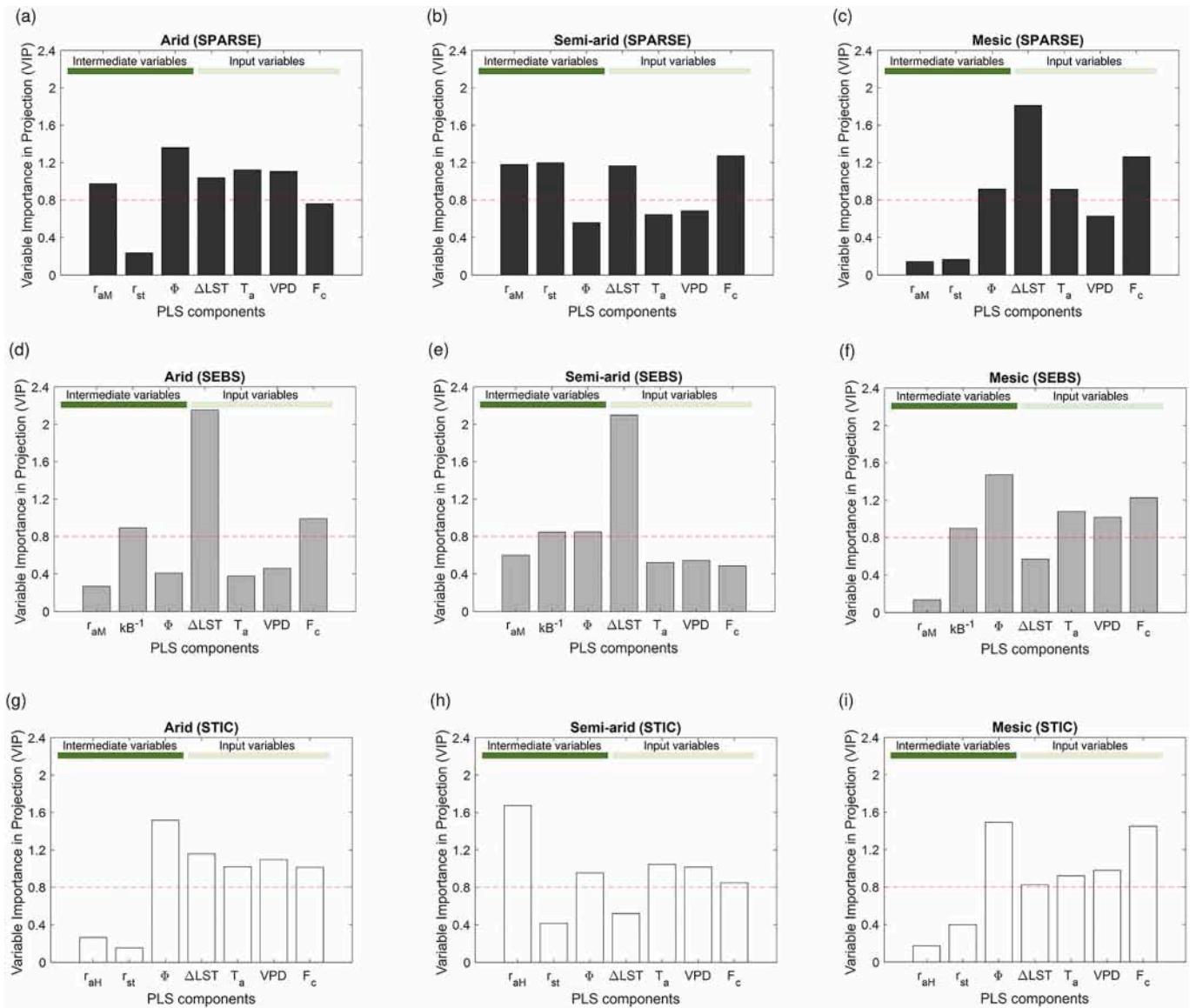
Fig. A2. (*continued*).

Fig. A3. Scatter plots of modelled net available energy *(Φ)* with SPARSE versus observed *Φ* for (a) Alice Springs, (b) Calperum, (c) Great Western Woodlands, (d) Gingin, (e) Sturt Plains, (f) Dry River, (g) Wombat, (h) Daly Uncleared and (i) Tumbarumba using MODIS *LST* as input to run the models.

Fig. A4. Bar plots of the Variable Importance in Projection (*VIP*) scores for the residual error of *H* involving r_{aM}, r_{aH}, kB^{-1} (SEBS), the stomata resistance (r_{st}) (SPARSE & STIC), modelled Φ with SPARSE, *LST* difference (ΔLST), air temperature (T_a), vapor pressure deficit (*VPD*) and F_c for SPARSE (a-c), SEBS (d-f) and STIC (g-i) for all the arid sites (clustered), semi-arid sites (clustered) and mesic sites (clustered) using MODIS *LST* as input to run the models. The dashed red line (VIP = 0.8) denotes the variable importance threshold. (For interpretation of the references to color in this figure legend, the reader is referred to the web version of this article.)
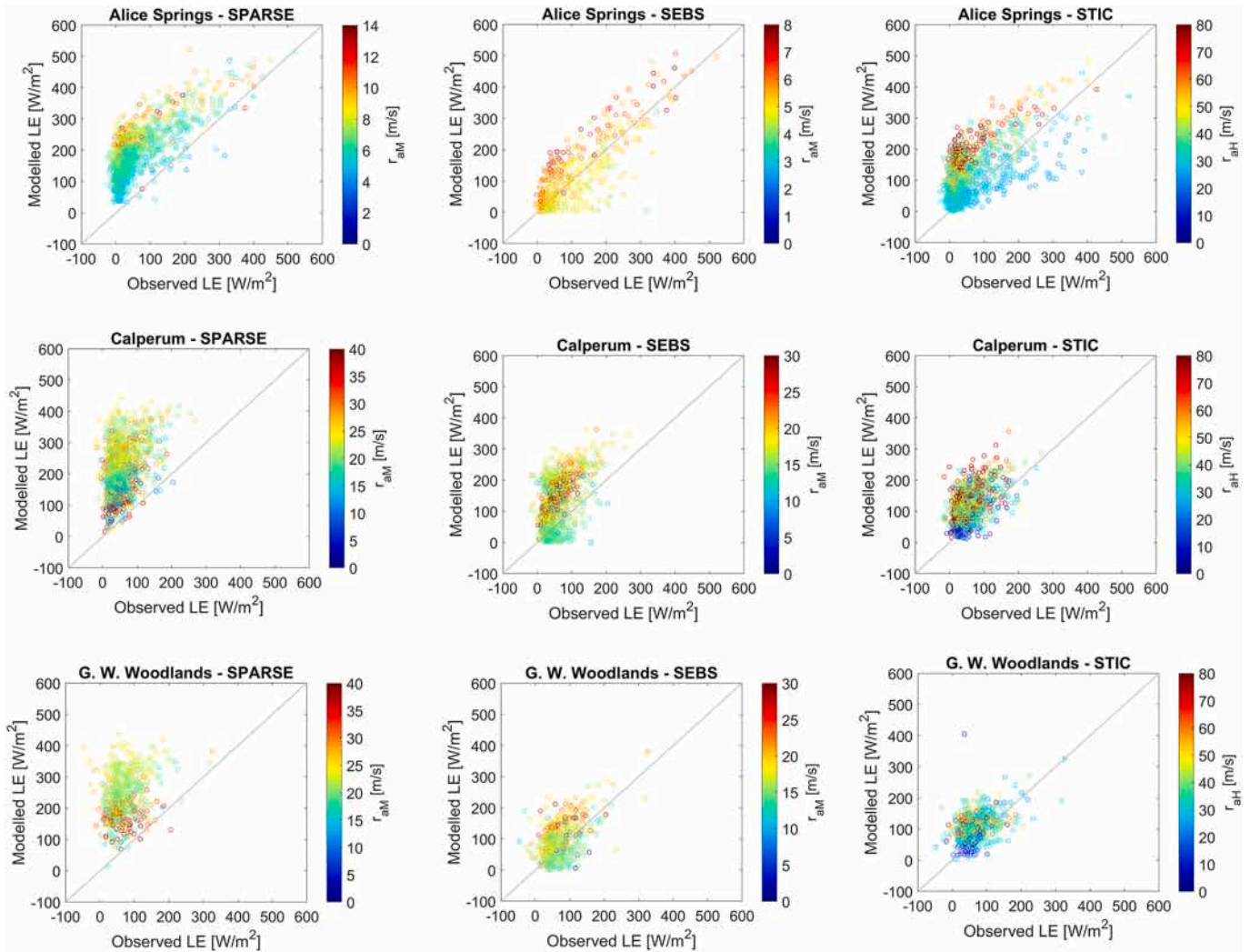
Fig. A5. Scatter plots of modelled *LE* versus observed *LE* color-coded with r_{aM} for SPARSE (left panel), SEBS (middle panel) and r_{aH} for STIC (right panel) for Alice Springs, Calperum, Great Western Woodlands, Gingin, Sturt Plains, Dry River, Wombat, Daly Uncleared and Tumbarumba using in-situ *LST* as input to run the models.
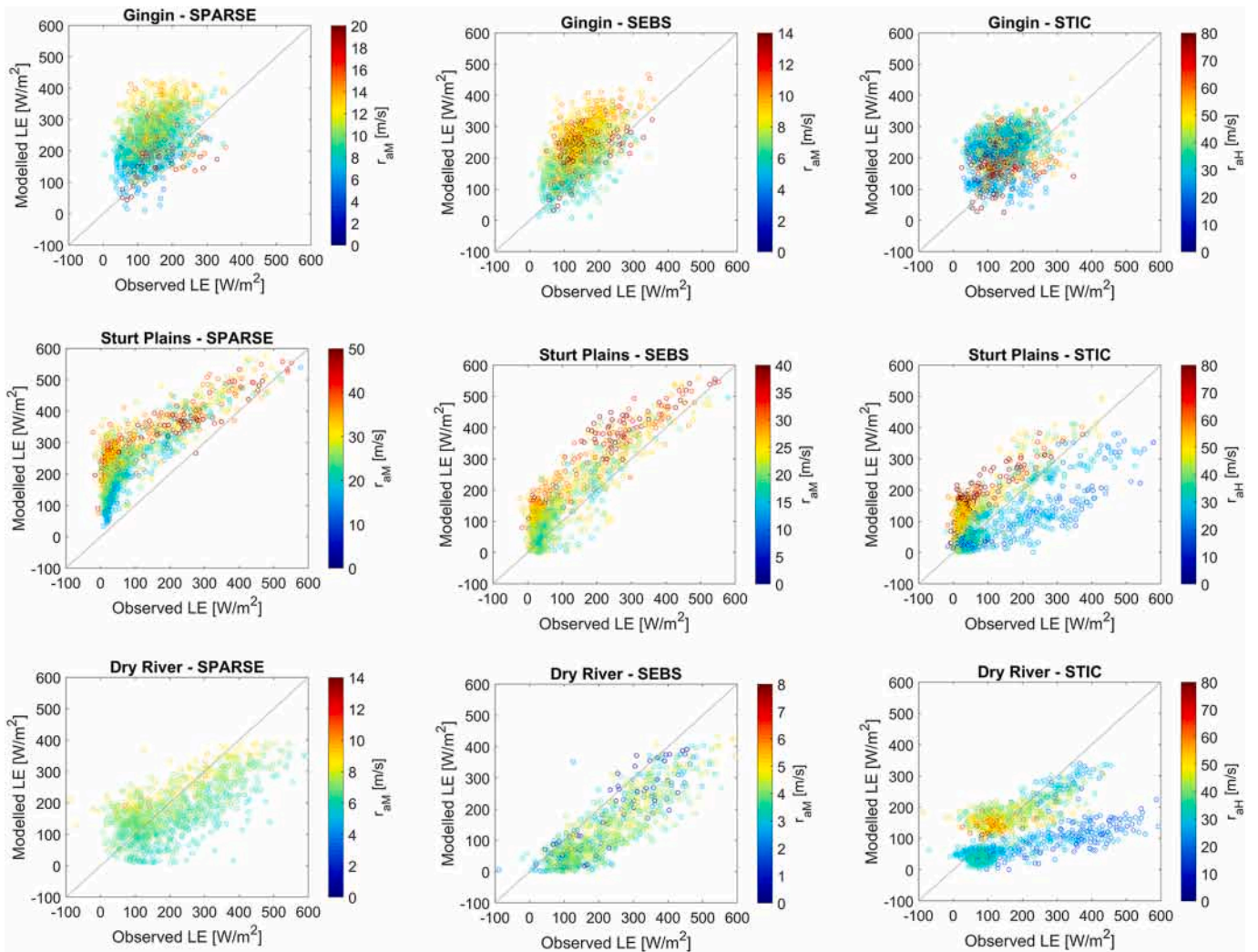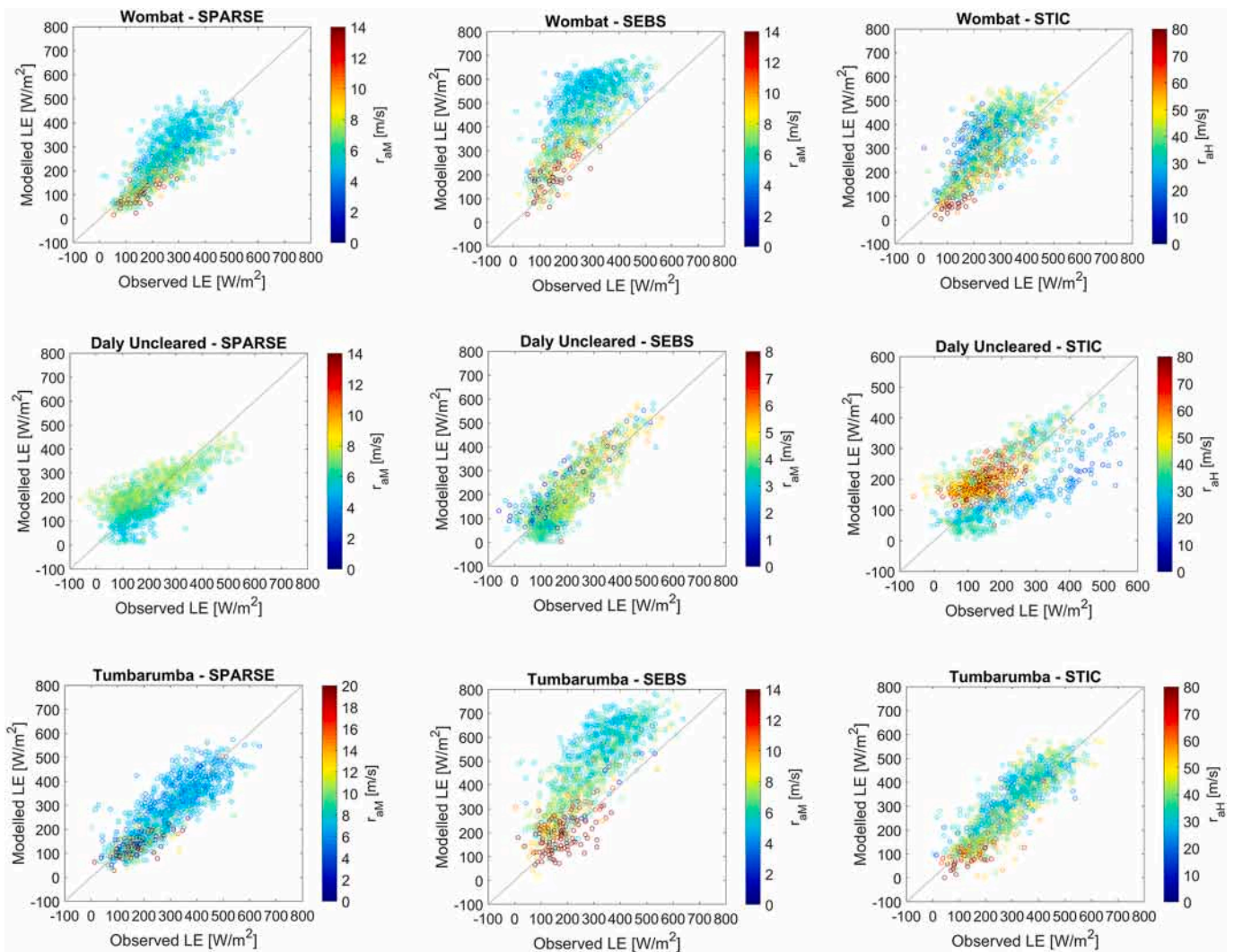
Fig. A5. (*continued*).

Fig. A5. (*continued*).

References

Anderson, M.C., Kustas, W.P., Norman, J.M., Hain, C.R., Mecikalski, J.R., Schultz, L., Gonzalez-Dugo, M.P., Cammalleri, C., d'Urso, G., Pimstein, A., Gao, F., 2011. Mapping daily evapotranspiration at field to continental scales using geostationary and polar orbiting satellite imagery. Hydrol. Earth Syst. Sci. 15, 223–239.

Bahir, M., Boulet, G., Olioso, A., Rivalland, V., Gallego-Elvira, B., Mira, M., Rodriguez, J. C., Jarlan, L., Merlin, O., 2017. Evaluation and aggregation properties of thermal infra-red-based evapotranspiration algorithms from 100 m to the km scale over a semi-arid irrigated agricultural area. Remote Sens. 9, 1178.

Banerjee, T., De Roo, F., Mauder, M., 2017. Explaining the convector effect in canopy turbulence by means of large-eddy simulation. Hydrol. Earth Syst. Sci. 21 (6), 2987–3000.

Beringer, J., Hutley, L.B., McHugh, I., Arndt, S.K., Campbell, D., Cleugh, H.A., Cleverly, J., Resco de Dios, V., Eamus, D., Evans, B., Ewenz, C., Grace, P., Griebel, A., Haverd, V., Hinko-Najera, N., Huete, A., Isaac, P., Kanniah, K., Leuning, R., Liddell, M.J., Macfarlane, C., Meyer, W., Moore, C., Pendall, E., Phillips, A., Phillips, R.L., Prober, S.M., Restrepo-Coupe, N., Rutledge, S., Schroder, I., Silberstein, R., Southall, P., Yee, M.S., Tapper, N.J., van Gorsel, E., Vote, C., Walker, J., Wardlaw, T., 2016. An introduction to the Australian and New Zealand flux tower network – OzFlux. Biogeosciences 13, 5895–5916.

Bhattarai, N., Mallick, K., Brunsell, N.A., Sun, G., Jain, M., 2018. Regional evapotranspiration from an image-based implementation of the surface temperature initiated closure (STIC1.2) model and its validation across an aridity gradient in the conterminous US. Hydrol. Earth Syst. Sci. 22, 2311–2341.

Boegh, E., Soegaard, H., Thomsen, A., 2002. Evaluating evapotranspiration rates and surface conditions using Landsat TM to estimate atmospheric resistance and surface resistance. Remote Sens. Environ. 79, 329–343.

Boulet, G., Olioso, A., Ceschia, E., Marloie, O., Coudert, B., Rivalland, V., Chirouze, J., Chehbouni, G., 2012. An empirical expression to relate aerodynamic and surface temperatures for use within single-source energy balance models. Agric. For. Meteorol. 161, 148–155.

Boulet, G., Mougenot, B., Lhomme, J.P., Fanise, P., Lili-Chabaane, Z., Olioso, A., Bahir, M., Rivalland, V., Jarlan, L., Merlin, O., Coudert, B., Er-Raki, S., Lagouarde, J. P., 2015. The SPARSE model for the prediction of water stress and evapotranspiration components from thermal infra-red data and its evaluation over irrigated and rainfed wheat. Hydrol. Earth Syst. Sci. 19, 4653–4672.

Bowman, D.M.J.S., Brown, G.K., Braby, M.F., Brown, J.R., Cook, L.G., Crisp, M.D., Ford, F., Haberle, S., Hughes, J., Isagi, Y., Joseph, L., McBride, J., Nelson, G., Ladiges, P.Y., 2010. Biogeography of the Australian monsoon tropics. J. Biogeogr. 37, 201–216.

Brutsaert, W., 1992. Stability correction functions for the mean wind speed and temperature in the unstable surface layer. Geophys. Res. Lett. 19, 469–472.

Brutsaert, W., 1999. Aspects of bulk atmospheric boundary layer similarity under free-convective conditions. Rev. Geophys. 37, 439–451.

Cai, W.J., van Rensch, P., Cowan, T., 2011a. Influence of global-scale variability on the subtropical ridge over Southeast Australia. J. Clim. 24, 6035–6053.

Cai, W.J., van Rensch, P., Cowan, T., Hendon, H.H., 2011b. Teleconnection pathways of ENSO and the IOD and the mechanisms for impacts on Australian rainfall. J. Clim. 24, 3910–3923.

Chen, J.M., Liu, J., 2020. Evolution of evapotranspiration models using thermal and shortwave remote sensing data. Remote Sens. Environ. 237.

Chen, X.L., Su, Z.B., Ma, Y.M., Yang, K., Wen, J., Zhang, Y., 2013. An improvement of roughness height parameterization of the surface energy balance system (SEBS) over the Tibetan plateau. J. Appl. Meteorol. Climatol. 52, 607–622.

Chen, X.L., Su, Z.B., Ma, Y.M., Cleverly, J., Liddell, M., 2017. An accurate estimate of monthly mean land surface temperatures from MODIS clear-sky retrievals. J. Hydrometeorol. 18, 2827–2847.

Chen, X.L., Massman, W.J., Su, Z.B., 2019a. A column canopy-air turbulent diffusion method for different canopy structures. J. Geophys. Res.-Atmos. 124, 488–506.

Chen, X.L., Su, Z.B., Ma, Y.M., Middleton, E.M., 2019b. Optimization of a remote sensing energy balance method over different canopy applied at global scale. Agric. For. Meteorol. 279, 15.

Chen, C., Li, D., Li, Y., Piao, S., Wang, X., Huang, M., Gentine, P., Nemani, R.R., Myneni, R.B., 2020. Biophysical impacts of earth greening largely controlled by aerodynamic resistance. Sci. Adv. 6 eabb1981.

Chong, I.G., Jun, C.H., 2005. Performance of some variable selection methods when multicollinearity is present. Chemom. Intell. Lab. Syst. 78, 103–112.

Choudhury, B.J., Monteith, J.L., 1988. A 4-layer model for heat-budget of homogeneous land surfaces. Q. J. R. Meteorol. Soc. 114, 373–398.

Choudhury, B.J., Idso, S.B., Reginato, R.J., 1987. Analysis of an empirical model for soil heat flux under a growing wheat crop for estimating evaporation by an infrared-temperature based energy balance equation. Agric. For. Meteorol. 39, 283–297.

Cleverly, J., Chen, C., Boulain, N., Villalobos-Vega, R., Faux, R., Grant, N., Yu, Q., Eamus, D., 2013. Aerodynamic resistance and Penman-Monteith evapotranspiration over a seasonally two-layered canopy in semiarid Central Australia. J. Hydrometeorol. 14, 1562–1570.

Cleverly, J., Eamus, D., Van Gorsel, E., Chen, C., Rumman, R., Luo, Q.Y., Coupe, N.R., Li, L.H., Kljun, N., Faux, R., Yu, Q., Huete, A., 2016. Productivity and evapotranspiration of two contrasting semiarid ecosystems following the 2011 global carbon land sink anomaly. Agric. For. Meteorol. 220, 151–159.

Colaizzi, P.D., Evett, S.R., Howell, T.A., Tolk, J.A., 2004. Comparison of aerodynamic and radiometric surface temperature using precision weighing lysimeters. In: Remote Sensing and Modeling of Ecosystems for Sustainability Proceedings of the Society of Photo-Optical Instrumentation Engineers. (Spie). Spie-Int Soc Optical Engineering, Bellingham, pp. 215–229.

de Jong, S., 1993. SIMPLS: an alternative approach to partial least squares regression. Chemom. Intell. Lab. Syst. 18, 251–263.

Foken, T., 2006. 50 years of the Monin-Obukhov similarity theory. Bound.-Layer Meteorol. 119, 431–447.

Foken, T., 2017. Micrometeorology, 2 ed. Springer, Berlin, Heidelberg.

Glenn, E.P., Doody, T.M., Guerschman, J.P., Huete, A.R., King, E.A., McVicar, T.R., Van Dijk, A., Van Niel, T.G., Yebra, M., Zhang, Y.Q., 2011. Actual evapotranspiration estimation by ground and remote sensing methods: the Australian experience. Hydrol. Process. 25, 4103–4116.

Gokmen, M., Vekerdy, Z., Verhoef, A., Verhoef, W., Batelaan, O., van der Tol, C., 2012. Integration of soil moisture in SEBS for improving evapotranspiration estimation under water stress conditions. Remote Sens. Environ. 121, 261–274.

Gokool, S., Riddell, E., Jarmain, C., Chetty, K., Feig, G., Thenga, H., 2020. Evaluating the accuracy of satellite-derived evapotranspiration estimates acquired during conditions of water stress. Int. J. Remote Sens. 41, 704–724.

González-Dugo, M.P., Chen, X., Andreu, A., Carpintero, E., Gómez-Giraldez, P.J., Carrara, A., Su, Z., 2020. Long-term water stress and drought monitoring of Mediterranean oak savanna vegetation using thermal remote sensing. Hydrol. Earth Syst. Sci. Discuss. 2020, 1–23.

Griebel, A., Bennett, L.T., Metzen, D., Cleverly, J., Burba, G., Arndt, S.K., 2016. Effects of inhomogeneities within the flux footprint on the interpretation of seasonal, annual, and interannual ecosystem carbon exchange. Agric. For. Meteorol. 221, 50–60.

Haghighi, E., Kirchner, J.W., 2017. Near-surface turbulence as a missing link in modeling evapotranspiration-soil moisture relationships. Water Resour. Res. 53, 5320–5344.

Haghighi, E., Or, D., 2015. Interactions of bluff-body obstacles with turbulent airflows affecting evaporative fluxes from porous surfaces. J. Hydrol. 530, 103–116.

Holwerda, F., Bruijnzeel, L.A., Scatena, F.N., Vugts, H.F., Meesters, A., 2012. Wet canopy evaporation from a Puerto Rican lower montane rain forest: the importance of realistically estimated aerodynamic conductance. J. Hydrol. 414, 1–15.

Isaac, P., Cleverly, J., McHugh, I., van Gorsel, E., Ewenz, C., Beringer, J., 2017. OzFlux data: network integration from collection to curation. Biogeosciences 14, 2903–2928.

Jarvis, P.G., McNaughton, K.G., 1986. Stomatal control of transpiration - scaling up from leaf to region. Adv. Ecol. Res. 15, 1–49.

Jimenez-Munoz, J.C., Sobrino, J.A., Gillespie, A., Sabol, D., Gustafson, W.T., 2006. Improved land surface emissivities over agricultural areas using ASTER NDVI. Remote Sens. Environ. 103, 474–487.

Jin, M.L., Liang, S.L., 2006. An improved land surface emissivity parameter for land surface models using global remote sensing observations. J. Clim. 19 (12), 2867–2881.

Knoben, W.J.M., Freer, J.E., Woods, R.A., 2019. Technical note: inherent benchmark or not? Comparing Nash-Sutcliffe and Kling-Gupta efficiency scores. Hydrol. Earth Syst. Sci. 23, 4323–4331.

Kustas, W., Anderson, M., 2009. Advances in thermal infrared remote sensing for land surface modeling. Agric. For. Meteorol. 149, 2071–2081.

Kustas, W.P., Anderson, M.C., Norman, J.M., Li, F.Q., 2007. Utility of radiometric-aerodynamic temperature relations for heat flux estimation. Bound.-Layer Meteorol. 122, 167–187.

Kustas, W.P., Nieto, H., Morillas, L., Anderson, M.C., Alfieri, J.G., Hipps, L.E., Villagarcia, L., Domingo, F., Garcia, M., 2016. Revisiting the paper "using radiometric surface temperature for surface energy flux estimation in Mediterranean drylands from a two-source perspective". Remote Sens. Environ. 184, 645–653.

Lee, T.R., Buban, M., 2020. Evaluation of Monin–Obukhov and Bulk Richardson parameterizations for surface–atmosphere exchange. J. Appl. Meteorol. Climatol. 59, 1091–1107.

Lhomme, J.P., Montes, C., Jacob, F., Prevot, L., 2012. Evaporation from heterogeneous and sparse canopies: on the formulations related to multi-source representations. Bound.-Layer Meteorol. 144, 243–262.

Li, Y., Kustas, W.P., Huang, C.L., Nieto, H., Haghighi, E., Anderson, M.C., Domingo, F., Garcia, M., Scott, R.L., 2019. Evaluating soil resistance formulations in thermal-based two-source energy balance (TSEB) model: implications for heterogeneous semiarid and arid regions. Water Resour. Res. 55, 1059–1078.

Liao, W.L., Rigden, A.J., Li, D., 2018. Attribution of local temperature response to deforestation. J. Geophys. Res. Biogeosci. 123, 1572–1587.

Liu, S.M., Lu, L., Mao, D., Jia, L., 2007. Evaluating parameterizations of aerodynamic resistance to heat transfer using field measurements. Hydrol. Earth Syst. Sci. 11, 769–783.

Mallick, K., Jarvis, A.J., Boegh, E., Fisher, J.B., Drewry, D.T., Tu, K.P., Hook, S.J., Hulley, G., Ardo, J., Beringer, J., Arain, A., Niyogi, D., 2014. A surface temperature initiated closure (STIC) for surface energy balance fluxes. Remote Sens. Environ. 141, 243–261.

Mallick, K., Boegh, E., Trebs, I., Alfieri, J.G., Kustas, W.P., Prueger, J.H., Niyogi, D., Das, N., Drewry, D.T., Hoffmann, L., Jarvis, A.J., 2015. Reintroducing radiometric surface temperature into the Penman-Monteith formulation. Water Resour. Res. 51, 6214–6243.

Mallick, K., Trebs, I., Boegh, E., Giustarini, L., Schlerf, M., Drewry, D.T., Hoffmann, L., von Randow, C., Kruijt, B., Araujo, A., Saleska, S., Ehleringer, J.R., Domingues, T.F., Ometto, J., Nobre, A.D., de Moraes, O.L.L., Hayek, M., Munger, J.W., Wofsy, S.C., 2016. Canopy-scale biophysical controls of transpiration and evaporation in the Amazon Basin. Hydrol. Earth Syst. Sci. 20, 4237–4264.

Mallick, K., Toivonen, E., Trebs, I., Boegh, E., Cleverly, J., Eamus, D., Koivusalo, H., Drewry, D., Arndt, S.K., Griebel, A., Beringer, J., Garcia, M., 2018a. Bridging thermal infrared sensing and physically-based evapotranspiration modeling: from theoretical implementation to validation across an aridity gradient in Australian ecosystems. Water Resour. Res. 54, 3409–3435.

Mallick, K., Wandera, L., Bhattarai, N., Hostache, R., Kleniewska, M., Chormanski, J., 2018b. A critical evaluation on the role of aerodynamic and canopy-surface conductance parameterization in SEB and SVAT models for simulating evapotranspiration: a case study in the upper Biebrza National Park Wetland in Poland. Water 10.

Marcolla, B., Cescatti, A., 2018. Geometry of the hemispherical radiometric footprint over plant canopies. Theor. Appl. Climatol. 134, 981–990.

Massman, W.J., Weil, J.C., 1999. An analytical one-dimensional second-order closure model of turbulence statistics and the Lagrangian time scale within and above plant canopies of arbitrary structure. Bound.-Layer Meteorol. 91, 81–107.

Mauder, M., Foken, T., Cuxart, J., 2020. Surface-energy-balance closure over land: a review. Bound.-Layer Meteorol. 177, 395–426.

Morillas, L., Garcia, M., Nieto, H., Villagarcia, L., Sandholt, I., Gonzalez-Dugo, M.P., Zarco-Tejada, P.J., Domingo, F., 2013. Using radiometric surface temperature for surface energy flux estimation in Mediterranean drylands from a two-source perspective. Remote Sens. Environ. 136, 234–246.

Norman, J.M., Kustas, W.P., Humes, K.S., 1995. Source approach for estimating soil and vegetation energy fluxes in observations of directional radiometric surface temperature. Agric. For. Meteorol. 77, 263–293.

Novick, K.A., Katul, G.G., 2020. The duality of reforestation impacts on surface and air temperature. J. Geophys. Res. Biogeosci. 125.

Panwar, A., Renner, M., Kleidon, A., 2020. Imprints of evaporative conditions and vegetation type in diurnal temperature variations. Hydrol. Earth Syst. Sci. 24, 4923–4942.

Pardo, N., Sanchez, M.L., Timmermans, J., Su, Z.B., Perez, I.A., Garcia, M.A., 2014. SEBS validation in a Spanish rotating crop. Agric. For. Meteorol. 195, 132–142.

Paul, G., Gowda, P.H., Prasad, P.V.V., Howell, T.A., Aiken, R.M., Neale, C.M.U., 2014. Investigating the influence of roughness length for heat transport (z(oh)) on the performance of SEBAL in semi-arid irrigated and dryland agricultural systems. J. Hydrol. 509, 231–244.

Payero, J.O., Neale, C.M.U., Wright, J.L., 2006. Effect of stability correction on remote sensing estimates of near-noon sensible heat flux of alfalfa and tall fescue grass. Int. J. Remote Sens. 27, 307–328.

Pereira, L.S., Perrier, A., Allen, R.G., Alves, I., 1999. Evapotranspiration: concepts and future trends. J. Irrig. Drain. Eng. 125, 45–51.

Raupach, M.R., 2001. Combination theory and equilibrium evaporation. Q. J. R. Meteorol. Soc. 127, 1149–1181.

Saadi, S., Boulet, G., Bahir, M., Brut, A., Delogu, E., Fanise, P., Mougenot, B., Simonneaux, V., Chabaane, Z.L., 2018. Assessment of actual evapotranspiration over a semiarid heterogeneous land surface by means of coupled low-resolution remote sensing data with an energy balance model: comparison to extra-large aperture scintillometer measurements. Hydrol. Earth Syst. Sci. 22, 2187–2209.

Seneviratne, S.I., Corti, T., Davin, E.L., Hirschi, M., Jaeger, E.B., Lehner, I., Orlowsky, B., Teuling, A.J., 2010. Investigating soil moisture-climate interactions in a changing climate: a review. Earth Sci. Rev. 99, 125–161.

Su, Z., 2002. The surface energy balance system (SEBS) for estimation of turbulent heat fluxes. Hydrol. Earth Syst. Sci. 6, 85–99.

Su, Z., Schmugge, T., Kustas, W.P., Massman, W.J., 2001. An evaluation of two models for estimation of the roughness height for heat transfer between the land surface and the atmosphere. J. Appl. Meteorol. 40, 1933–1951.

Sun, J.L., Takle, E.S., Acevedo, O.C., 2020. Understanding physical processes represented by the Monin-Obukhov bulk formula for momentum transfer. Bound.-Layer Meteorol. 177, 69–95.

Troufleau, D., Lhomme, J.P., Monteny, B., Vidal, A., 1997. Sensible heat flux and radiometric surface temperature over sparse Sahelian vegetation .1. An experimental analysis of the kB-1 parameter. J. Hydrol. 188, 815–838.

Twine, T.E., Kustas, W.P., Norman, J.M., Cook, D.R., Houser, P.R., Meyers, T.P., Prueger, J.H., Starks, P.J., Wesely, M.L., 2000. Correcting eddy-covariance flux underestimates over a grassland. Agric. For. Meteorol. 103, 279–300.

van der Kwast, J., Timmermans, W., Gieske, A., Su, Z., Olioso, A., Jia, L., Elbers, J., Karssenberg, D., de Jong, S.M., 2009. Evaluation of the surface energy balance system (SEBS) applied to ASTER imagery with flux-measurements at the SPARC 2004 site (Barrax, Spain). Hydrol. Earth Syst. Sci. 13, 1337–1347.

van Dijk, A., Gash, J.H., van Gorsel, E., Blanken, P.D., Cescatti, A., Emmel, C., Gielen, B., Harman, I.N., Kiely, G., Merbold, L., Montagnani, L., Moors, E., Sottocornola, M., Varlagin, A., Williams, C.A., Wohlfahrt, G., 2015. Rainfall interception and the coupled surface water and energy balance. Agric. For. Meteorol. 214, 402–415.

van Gorsel, E., Wolf, S., Cleverly, J., Isaac, P., Haverd, V., Ewenz, C., Arndt, S., Beringer, J., de Dios, V.R., Evans, B.J., Griebel, A., Hutley, L.B., Keenan, T., Kljun, N., Macfarlane, C., Meyer, W.S., McHugh, I., Pendall, E., Prober, S.M., Silberstein, R., 2016. Carbon uptake and water use in woodlands and forests in southern Australia during an extreme heat wave event in the "angry summer" of 2012/2013. Biogeosciences 13, 5947–5964.

Verma, S.B., 1989. Aerodynamic Resistances to Transfers of Heat, Mass and Momentum. IAHS Pub. No. 177, pp. 13–20.

Vivoni, E.R., Watts, C.J., Rodriguez, J.C., Garatuza-Payan, J., Mendez-Barroso, L.A., Saiz-Hernandez, J.A., 2010. Improved land-atmosphere relations through distributed footprint sampling in a subtropical scrubland during the North American monsoon. J. Arid Environ. 74, 579–584.

Winckler, J., Reick, C.H., Bright, R.M., Pongratz, J., 2019. Importance of surface roughness for the local biogeophysical effects of deforestation. J. Geophys. Res.-Atmos. 124, 8605–8618.

Zhou, Y.L., Ju, W.M., Sun, X.M., Wen, X.F., Guan, D.X., 2012. Significant decrease of uncertainties in sensible heat flux simulation using temporally variable aerodynamic roughness in two typical Forest ecosystems of China. J. Appl. Meteorol. Climatol. 51, 1099–1110.